
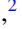



Coherent excitation transport through ring-shaped networks

Francesco Perciavalle ^{1,2}, Oliver Morsch,³ Davide Rossini ², and Luigi Amico ^{1,4,5}

¹*Quantum Research Center, Technology Innovation Institute, P.O. Box 9639, Abu Dhabi, UAE*

²*Dipartimento di Fisica dell'Università di Pisa and INFN, Largo Pontecorvo 3, I-56127 Pisa, Italy*

³*CNR-INO and Dipartimento di Fisica dell'Università di Pisa, Largo Pontecorvo 3, I-56127 Pisa, Italy*

⁴*Dipartimento di Fisica e Astronomia "Ettore Majorana", University of Catania, Via S. Sofia 64, I-95123 Catania, Italy*

⁵*INFN-Sezione di Catania, Via S. Sofia 64, I-95123 Catania, Italy*



(Received 18 January 2024; revised 18 April 2024; accepted 22 May 2024; published 25 June 2024)

The coherent quantum transport of matter wave through a ring-shaped circuit attached to leads defines an iconic system in mesoscopic physics that has allowed researchers to both explore fundamental questions in quantum science and to draw important avenues for conceiving devices of practical use. Here we study the source-to-drain transport of excitations going through a ring network, without propagation of matter waves. We model the circuit in terms of a spin system with specific long-range interactions that are relevant for quantum technology, such as Rydberg atoms trapped in optical tweezers or ion traps. Inspired by the logic of rf- and dc-SQUIDS, we consider rings with one and two local energy offsets, or detunings. As a combination of specific phase shifts in going through the localized detunings and as a result of coherent tunneling, we demonstrate how the transport of excitations can be controlled, with a distinctive dependence on the range of interactions.

DOI: [10.1103/PhysRevA.109.062619](https://doi.org/10.1103/PhysRevA.109.062619)

I. INTRODUCTION

Quantum transport in mesoscopic circuits deals with matter propagating in networks characterized by a spatial scale comparable with the particle's coherence length [1,2]. In this regime, quantum effects such as quantum tunneling, conductance quantization, flux quantization, Aharonov-Bohm effect, etc. play a prominent role [3–5]. Recently, the transport properties of cold atoms guided in versatile and flexible laser-generated circuits have been studied both theoretically and experimentally [6–13]. In fact, through widely tunable interactions and disorder, new paradigms in mesoscopic physics have been defined, for both bosonic and fermionic systems, with a great potential for basic quantum science and applications [14,15].

In this paper, we refer to one of the most iconic systems of mesoscopic physics that has led to far-reaching implications: a mesoscopic ring-shaped track connected to source and drain leads [1,2,16–18]. The tunneling through scattering impurities or localized barriers placed in the ring circuit can induce specific phase shifts in the particles wave function [19]. In this way, the source-to-drain current can be controlled, a fact that is relevant to study the fundamental features of quantum interference and to engineer mesoscopic quantum devices with enhanced performances. With a similar logic, neutral bosonic matter-wave current oscillations have been predicted and analyzed in Ref. [10]. Rings with one or two localized barriers can define the bosonic analog of rf- and dc- superconducting quantum interference devices (SQUIDS) [15,20–22]. Such cold-atom implementations pave the way to rotation sensors based on the Sagnac effect [23].

Here we study the source-to-drain quantum transport through a ring-shaped circuit, in which the dynamics occur in terms of excitations, rather than of matter. The implemen-

tation we rely on is a circuit made of Rydberg atoms trapped in tweezers or ions trapped in suitable electromagnetic fields [24–27]. Indeed, in such systems, the motion of the atoms or of the ions can be neglected, with the relevant dynamics occurring as the transfer of excitations of internal energy states. Moreover, both Rydberg atoms and ions can be trapped in a large variety of different geometries and with a remarkable control of the physical conditions [28–31]. In contrast to the cases considered so far, here we deal with systems with a long-range interaction, capturing the characteristic physics of Rydberg atoms and trapped ions [32–34].

We implement a specific quench dynamics that we demonstrate to lead to the sought drain-to-source excitation transport: after initializing the excitation in the source, it propagates along the two arms of the ring and, after many scattering events determined by the interaction, reaches the drain. Dealing with a closed system, the excitations population in the source and in the drain displays characteristic oscillations. We shall demonstrate that the entire excitation dynamics and then the source-to-drain transport can be controlled by suitable energy level detunings localized in the ring track. Such detunings play a similar role of what the aforementioned local potential barriers do for matter waves [10]. Indeed, the presence of detunings gives a nontrivial time-dependent phase to the time-evolved state. Inspired by the rf- and dc-SQUID concepts, we address the cases of one and two localized detunings. The paper is organized as follows: In Sec. II, we introduce the model and the possible experimental platforms on which it can be realized. In Sec. III, we study the dynamics of the leads and the ring population in the presence of a single detuning in one arm of the ring. In Sec. IV, we perform the same type of simulations, but in presence of two detunings, i.e., one for each arm of the ring, with the same height and the same sign first, and with opposite sign second.

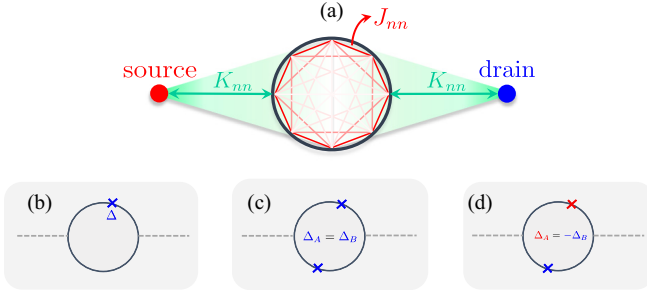


FIG. 1. (a) Pictorial representation of the system: two single-site leads, a source and a drain, are connected to a ring lattice. The various sites are connected with a hopping strength that scales as $1/d^\alpha$, with d the distance between sites. Intraring and leads-ring hopping strengths are denoted by J_{nn} (red lines) and K_{nm} (green lines), respectively. Boxes show the three possible configurations that we are going to study: (b) one barrier, (c) two barriers with the same sign, and (d) two barriers with opposite sign. The number N_r of sites in the ring lattice is such that N_r is even, while $N_r/2$ is odd. The asymmetric location of the detunings with respect to the leads is chosen to guarantee different paths for the excitation on the two arms.

Our conclusions are drawn in Sec. V. The Appendix provides a more detailed analysis of the model properties and of the mechanisms that lead to the peculiar dynamics observed in the main text.

II. MODEL AND METHODS

We consider a system comprised of two leads, the source (\mathcal{S}) and the drain (\mathcal{D}), each of them modeled by a single site containing, at most, one excitation, connected to a ring network (\mathcal{R}) of N_r sites. Localized detunings, or impurities (\mathcal{I}), are placed in the ring lattice and arranged in different configurations (see Fig. 1). The excitation in each site is modeled as a two-level atom system $\{|\uparrow\rangle, |\downarrow\rangle\}$. The system Hamiltonian reads

$$\hat{\mathcal{H}} = \hat{\mathcal{H}}_{\mathcal{R}} + \sum_{\mathcal{L}=\mathcal{S},\mathcal{D}} \hat{\mathcal{H}}_{\mathcal{L}\mathcal{R}} + \hat{\mathcal{H}}_{\mathcal{S}\mathcal{D}}, \quad (1)$$

with

$$\hat{\mathcal{H}}_{\mathcal{R}} = \sum_{i<j\in\mathcal{R}} \frac{g}{d_{i,j}^\alpha} (\hat{\sigma}_i^+ \hat{\sigma}_j^- + \text{H.c.}) + \hat{\mathcal{H}}_{\text{Det}}, \quad (2a)$$

$$\hat{\mathcal{H}}_{\mathcal{L}\mathcal{R}} = \sum_{j\in\mathcal{R}} \frac{g}{d_{\mathcal{L},j}^\alpha} (\hat{\sigma}_j^+ \hat{\sigma}_{\mathcal{L}}^- + \text{H.c.}) \quad (\mathcal{L} = \mathcal{S}, \mathcal{D}), \quad (2b)$$

$$\hat{\mathcal{H}}_{\mathcal{S}\mathcal{D}} = \frac{g}{d_{\mathcal{S},\mathcal{D}}^\alpha} (\hat{\sigma}_{\mathcal{S}}^+ \hat{\sigma}_{\mathcal{D}}^- + \text{H.c.}), \quad (2c)$$

$$\hat{\mathcal{H}}_{\text{Det}} = \sum_{j\in\mathcal{R}} \sum_{j_i\in\mathcal{I}} \Delta_j \hat{n}_j \delta_{j,j_i}. \quad (2d)$$

Here, $\hat{\sigma}_\ell^a$ ($a = x, y, z$) denote the spin-1/2 Pauli matrices on a given atom and $\hat{\sigma}_\ell^\pm = \frac{1}{2}(\hat{\sigma}_\ell^x \pm i\hat{\sigma}_\ell^y)$ are the corresponding raising and lowering operators, with $\ell = \{\mathcal{S}, \mathcal{D}, 1, \dots, N_r\}$ labeling one of the atoms in the leads or in the ring. The Hamiltonian part [Eq. (2a)] describes the intraring hopping in the presence of detunings [Eq. (2d)], while Eq. (2b) describes the leads-ring hopping and Eq. (2c) describes the

direct source-drain hopping. We suppose that the excitation $|\uparrow\rangle$ can hop from site to site with a strength scaling as $1/d^\alpha$, where d denotes the distance between the sites and $\alpha \geq 0$ is a parameter inversely related to the hopping range. In particular, $d_{i,j}$ is the intraring distance ($i, j = 1, \dots, N_r$), $d_{\mathcal{S},j}$ and $d_{\mathcal{D},j}$ are the distances between the leads and all the sites of the ring, while $d_{\mathcal{S},\mathcal{D}}$ is the distance between source and drain. Hereafter, we mainly concentrate on the weak lead-ring coupling limit, corresponding to $K_{nm} \ll J_{nn}$, where K_{nm} and J_{nn} are the leads-ring and intraring nearest-neighbor hopping strengths, respectively (see Appendix A for details). We also consider an even number N_r of atoms in the ring, in such a way that $N_r/2$ is odd.

We should stress that we are interested in the cases $1 \leq \alpha \leq 3$, where the nearest-neighbor and the fully connected models correspond to $\alpha \rightarrow \infty$ and $\alpha = 0$, respectively. Trapped ions in linear chains provide a powerful platform to realize quantum spin Hamiltonians in which the spin-spin interaction or the hopping strength scale approximately as $d^{-\alpha}$, where $\alpha \in (0, 3)$ [24,32,35–38]; the $|\downarrow\rangle$ and $|\uparrow\rangle$ states are two internal electronic states of the ions. The implementation of different geometries is more challenging, but two-dimensional spin Hamiltonians [37,39–43] as well as circular ring traps of ions [30,44,45] have already been realized. The case $\alpha = 3$ can also be implemented in Rydberg atoms. For such systems, $|\downarrow\rangle$ and $|\uparrow\rangle$ are two Rydberg states of opposite parity (i.e., $|S\rangle$ and $|P\rangle$) [26,33,46,47]. Thanks to the high control on the geometry in which the atoms are located in these systems [28,29,48], it is possible to realize ring-shaped and more complicated geometries [49].

We focus on three possible configurations of the localized detunings in the ring lattice. The case $\mathcal{I} = \{j_0\}$ corresponds to one localized detuning [Fig. 1(b)]; the path crossed by the excitation in the two arms of the ring is clearly different. The two other cases correspond to $\mathcal{I} = \{j_A, j_B\}$, with j_A and j_B in diametrical position, $\Delta_A = \Delta_B$ and $\Delta_A = -\Delta_B$, respectively [Figs. 1(c) and 1(d)]. Since $d_{\mathcal{S},j_A} \neq d_{\mathcal{S},j_B}$, also in this case, the path crossed by the excitation fraction in one arm of the ring is different from the other. The local detunings are experimentally feasible through local ac-Stark shifts with a focused laser on the site of interest [32,50].

To study the excitation transport, we apply the following quench protocol. At $t = 0$, we localize a single excitation in the source,

$$|\psi(0)\rangle = |\uparrow\rangle_{\mathcal{S}} \otimes |\downarrow, \dots, \downarrow\rangle_{\mathcal{R}} \otimes |\downarrow\rangle_{\mathcal{D}}; \quad (3)$$

then we evolve the state via the Schrödinger equation $|\psi(t)\rangle = \exp(-i\hat{\mathcal{H}}t)|\psi(0)\rangle$. To monitor the dynamics, we scrutinize the number of excitations in the source, the ring, and the drain,

$$\hat{n}_{\mathcal{R}} = \frac{1}{2} \sum_{j\in\mathcal{R}} (\hat{1}_j + \hat{\sigma}_j^z), \quad \hat{n}_{\mathcal{L}} = \frac{1}{2} (\hat{1}_{\mathcal{L}} + \hat{\sigma}_{\mathcal{L}}^z) \quad (\mathcal{L} = \mathcal{S}, \mathcal{D}). \quad (4)$$

Since the Hamiltonian conserves the total number of excitations, $\hat{n}_{\text{tot}} = \hat{n}_{\mathcal{S}} + \hat{n}_{\mathcal{R}} + \hat{n}_{\mathcal{D}}$, with the initial condition (3), we can work in the one-excitation sector, namely, $\langle\psi(t)|\hat{n}_{\text{tot}}|\psi(t)\rangle = 1$. Thus, we define the projector \hat{P} represented by a $N \times 2^N$ matrix that projects operators and states

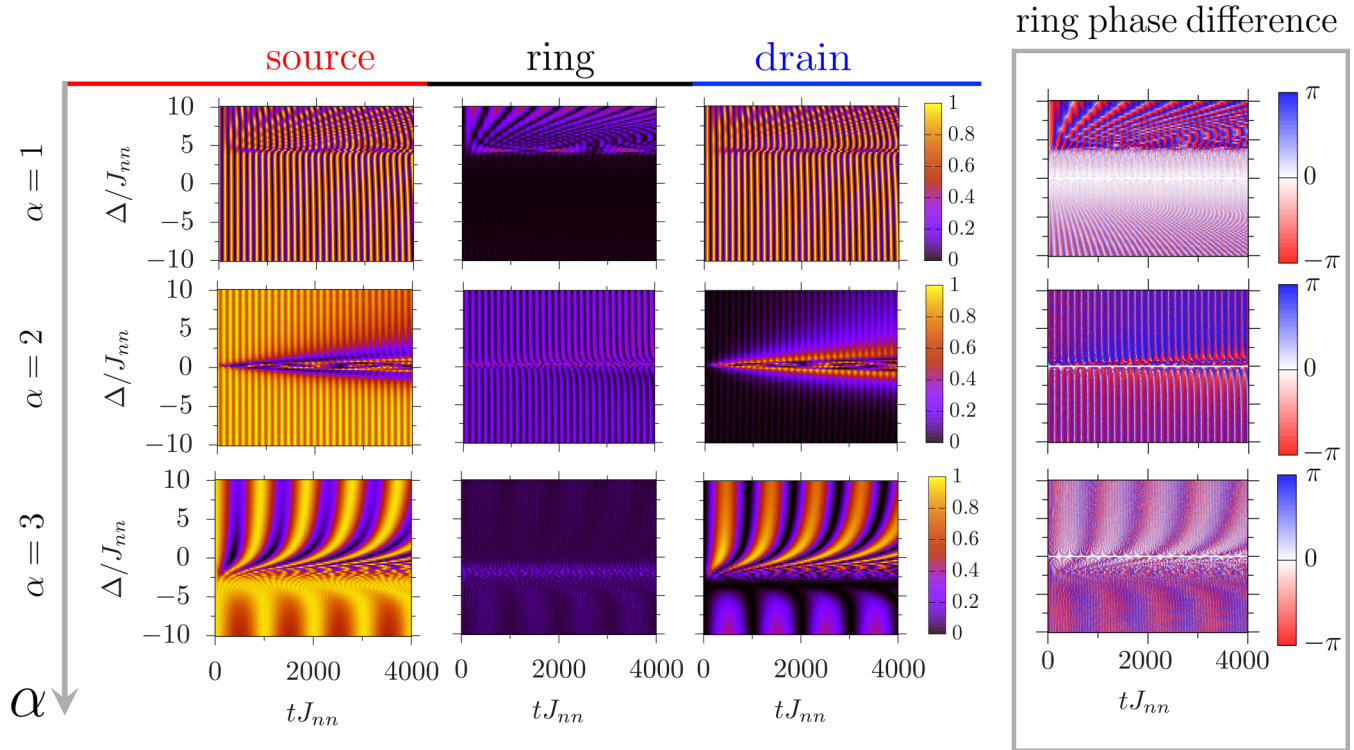


FIG. 2. Left panels: Excitation populations in the source P_S , the ring P_R , and the drain P_D , for three different values of the hopping range $\alpha = 1, 2, 3$, from top to bottom. Right panels: Ring phase difference $\delta\phi$ between two opposite sites located in the two arms of the ring, for the three values of α considered. Excitation populations and phase difference are plotted as a function of time (x axis) and detuning (y axis) of the single barrier located in the ring at position $j_0 = \lceil N_r/4 \rceil$. The population values are indicated by the color bar that goes from 0 to 1, and the phase difference by the one that goes from $-\pi$ to π . The number of sites in the ring is $N_r = 14$. The leads-ring coupling is $K_m = J_m/10$

of the full Hilbert space into operators and states of the one-excitation sector. The states and operators with which we will work are of the form $\hat{P}|\psi\rangle$ and $\hat{P}\hat{O}\hat{P}^\dagger$, with $|\psi\rangle$ and \hat{O} being a generic state and operator acting on the full Hilbert space.

Numerical computations have been performed using the JULIA package QUANTUMOPTICS.JL [51].

III. DYNAMICS IN THE PRESENCE OF A SINGLE DETUNING

Let us first consider the case of a single localized detuning [Fig. 1(b)]. We analyze the dynamics of the number of excitations in the source, the ring, and the drain, as well as the phase difference behavior between the two arms of the ring (in particular, the phase difference between two opposite sites located in the two different arms). Numerical results are summarized in Fig. 2.

A. Excitation dynamics

Because of the weak-coupling assumption, insight on the general features of the excitation dynamics can be achieved by looking at the (discrete) energy spectrum of the leads and the ring separately. The initial state $|\psi(0)\rangle \equiv |S\rangle$ is assumed to be at zero energy. The ring Hamiltonian in the single-particle sector has N_r eigenstates with nonzero energies; they result to be doubly degenerate, except for the ground state and the

highest excited state. The role of the localized detuning is to break the degeneracies and shift the ring levels. For specific values of the detuning Δ_{res} , the ring energy levels can be resonant with the initial source state $|S\rangle$ (see Appendix B). In this case, the excitation is transferred from the source to the drain and backward to the source, through the ring that is well populated (Fig. 2, left panels). Since the total number of excitations is conserved and the ring is populated, during its time evolution the population is distributed along the leads and the channel. Far from resonance, coherent source-drain oscillations display a marked dependence on Δ as soon as α increases. This means that the source-drain dynamics depends on the characteristics of the ring and not only on the source-drain direct coupling \hat{H}_{SD} . In this regime, the transport can occur in terms of cotunneling processes [4,52,53]: Similarly to the transport occurring in quantum dots in the regime in which sequential tunneling cannot happen (because of the Coulomb blockade), here a source-to-drain transport can occur through virtual transitions in the ring energy levels; in this regime, the ring is found with a low population of excitations.

Due to the presence of more than nearest-neighbor hopping processes, specific features of the system emerge when the leads and the ring-shaped track are not treated separately (see Fig. 1). Specifically, because of a combination of geometrical effects and energy level configuration, we found that the transport displays a marked dependence on α , especially in the (leads-ring) nearly resonant regimes.

For $\alpha = 1$, the source and drain populations oscillate regularly until $\Delta/J_{nn} \approx 5$, corresponding to the value for which the rings start to be populated and the dynamics inside the leads is less regular. The specific detuning values for which the ring is populated correspond to those for which the ring is resonant with the leads (see Fig. 7 in Appendix B 2). Far from those values, the ring is not populated and the source-drain oscillations do not depend on the detuning. A peculiar localization phenomenon related to the emergence of a source localized eigenstate (see Appendix D) is observed for small negative values of the detuning. An appropriate quench of the detuning from negative to positive can be used to switch from no-transfer to almost perfect transfer of excitations.

For $\alpha = 2$, the dynamics is quite different: in the (Δ, t) plane, a V pattern appears. On the borders of the V pattern, the drain and source populations are, respectively, maximum and minimum. The vertex of the V is in correspondence with Δ_{res} , where the ring is more populated. Another important feature of this regime is the population dynamics for values of detuning far from the resonance. The source is, at every time, the most populated, and the drain is the less populated. The ring population is small but not zero; it shows a weak oscillation with those of the source.

The $\alpha = 3$ regime is characterized by slow (compared with the previous cases $\alpha = 1$ and $\alpha = 2$) coherent transfer of excitation from the source to the drain, interrupted at the value of Δ for which the source and ring are resonant. As a specific feature of this case, we note a localization of the excitation in the source occurring for values of Δ slightly smaller than Δ_{res} . Indeed, such localized source state appears in the analysis of the full leads-ring system Hamiltonian spectrum (see Appendix D). For different values of Δ , the complete states also have a substantial projection in the drain state and therefore the dynamics results display the characteristic source-drain coherent oscillations.

B. Phase difference dynamics

We now analyze the phase of the excitations flow between the two arms of the ring. To this end, we compute the phase difference between the two symmetric sites of the arms, labeled by $i = N_r/2 - 1$ and $j = N_r/2 + 1$. The argument of the two-body correlator $\langle \hat{\sigma}_i^+ \hat{\sigma}_j^- \rangle$ gives the phase difference $\delta\phi$ between the two sites (see Appendix E for details). To corroborate our results, we analytically studied a straight finite chain and found that the phases of the coefficients of the time-evolved state in the position basis nontrivially depend on Δ .

The rightmost panels of Fig. 2 report the phase difference as a function of time and detuning, for various values of α . Our results indicate that as for matter waves with a localized potential barrier, the localized detuning causes a phase shift between the two arms of the ring. The dependence of the phase difference on the detuning is evident for any α . In particular, it follows the oscillation frequency of the ring population. However, even when such oscillation amplitude is small and hardly observable, the phase difference can present non-negligible oscillations. For instance, for $\alpha = 1$ and a negative detuning, there are evident phase difference oscillations

while the ring is basically not populated. In a window around $\Delta = 0$, the phase difference is zero because the paths on the two arms are the same. On the other hand, in correspondence with the resonances, as soon as the ring becomes populated, we observe strong oscillations in the phase difference. In general, phase oscillations follow the population ones, independently of the amplitude of the latter. If there is a small amount of excitations moving in the ring, the phase difference oscillates with an amplitude that is significantly different from zero.

IV. DYNAMICS IN THE PRESENCE OF DOUBLE DETUNING

In this section, we focus on the source-to-drain dynamics of the number of excitations in the case in which two atoms in the ring are detuned. We first study the case in which the two detunings have the same sign [Fig. 1(c)] and then the case in which they have same magnitude but opposite sign [Fig. 1(d)].

A. Excitation dynamics in the presence of double detunings with the same sign

Also in this case, the hopping range has pronounced effects on the dynamics. The combined energy shifts caused by the two detunings and hopping range give rise to a resonant transport occurring in correspondence to two resonances (instead of the one in the previous single-detuning case) that turns out to not be symmetric with respect to $\Delta = 0$. The nature of the level shift that brings to resonance can be accessed analytically and numerically looking at the ring spectrum, respectively, in the nearest-neighbor and long-range cases (see Appendix B). The population dynamics is reported in the left panels of Fig. 3.

For $\alpha = 1$, the dynamics is characterized by fast oscillations between source and drain, with a frequency that is nearly independent of the detuning. The ring is almost never populated except for the two Δ_{res} values, where the dynamics in the leads is erratic. In the case $\alpha = 2$, the dynamics clearly changes. Far from resonances, the dynamics is similar to the one observed in the single-detuning case. In this case, we see two V-shaped patterns in the (Δ, t) plane around the two resonances. We notice a depletion in the source and a filling of the drain in correspondence to the meeting points of the two V-shaped patterns. Finally, as in the case with single detuning, for $\alpha = 3$, the transport between source and drain is slower and more affected by the process occurring in the ring track. In particular, by tuning Δ , the transport in the system shows markedly different features. For large (positive or negative) values of Δ , the transport of excitations is slowed down, with the ring being weakly populated. Around the two resonant levels, the transport becomes erratic and the ring becomes populated. In between the two resonances, we observe regular and fast oscillations of the population in the leads.

In Appendix F, we report strong leads-ring coupling results for $\alpha = 3$. We observe that for increasing K_{nn}/J_{nn} , the source-drain oscillations weaken. The latter survive until K_{nn} remains smaller than J_{nn} ; when the couplings are comparable,

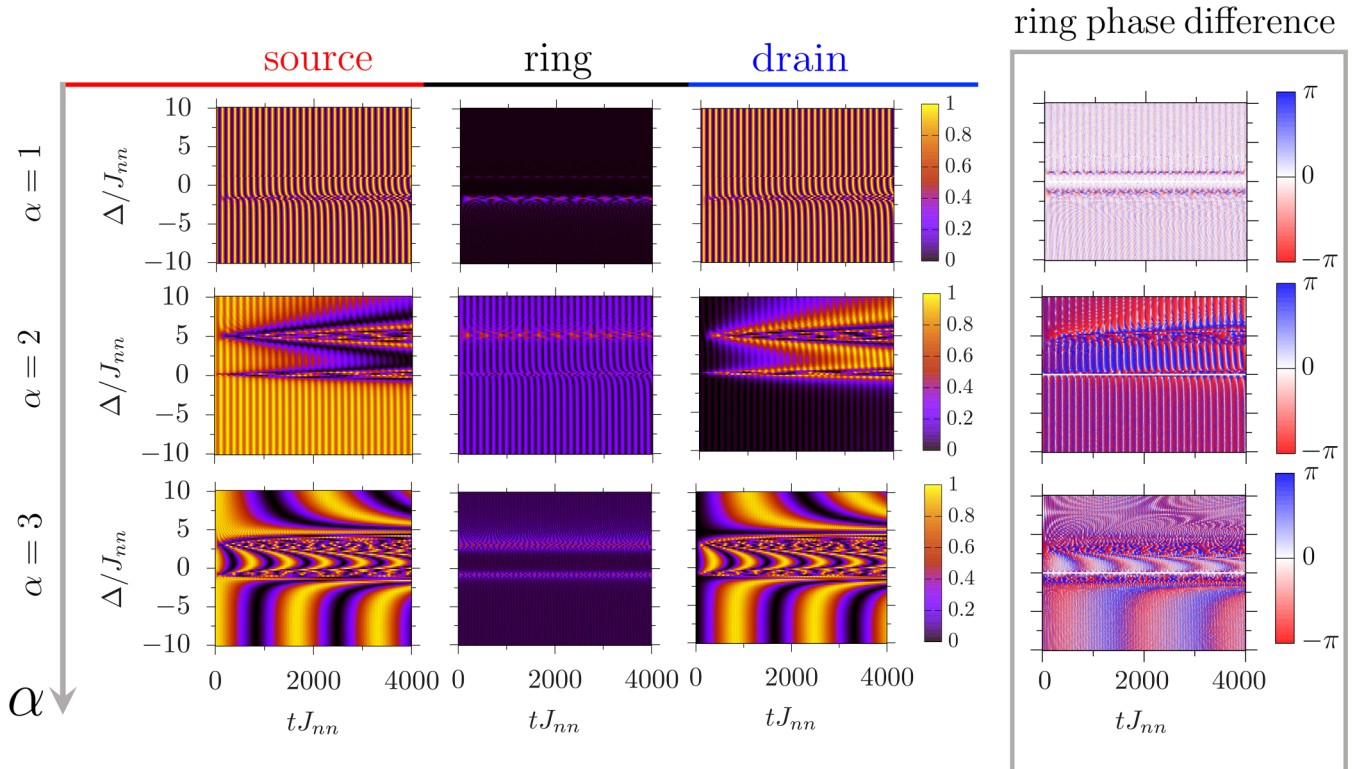


FIG. 3. Populations and ring phase difference as in Fig. 2, for two equal detunings ($\Delta_A = \Delta_B = \Delta$) located at $j_A = \lceil N_r/4 \rceil$ and $j_B = \lceil 3N_r/4 \rceil$. The Hamiltonian parameters are set as in Fig. 2.

the leads are weakly populated and clear oscillations are no longer observed. In this scheme, the spectrum is not divided into leads and ring states far from the resonance, so the ring is populated independently of Δ_{res} .

B. Excitation dynamics in the presence of double detunings with opposite sign

We complete our analysis by studying the configuration of a double equal barrier with opposite sign. Also here, the three different regimes can be observed by changing α . The double-barrier regime is basically different from the other two because the first perturbative order energy correction is zero (see Appendix B), and thus it is harder to get resonances. Results for the population dynamics are reported in the left panels of Fig. 4.

For $\alpha = 1$, the dynamics is characterized by fast oscillations between source and drain; the ring is never resonant with the initial state and so is never populated. For $\alpha = 2$, the ring spectrum presents two symmetric resonances (instead of the asymmetric ones of the previous section) with the zero-energy mode. This feature is corroborated by a perturbative analysis showing that the resonances depends on Δ^2 (see Appendix B). For large (positive and negative) values of Δ , the population in the drain is minimal, while a small fraction of excitation oscillates between source and ring. For values of Δ between the two resonances, a source-drain slow oscillation given by the recombination of the two V-shaped patterns appears. The regime corresponding to $\alpha = 3$ is characterized by slow coherent oscillations between the two leads, with the ring track being weakly populated. Differently from the $\alpha = 1$ case,

the value of Δ determines the oscillation frequency between source and drain. We found that the excitation transfer slows down by increasing Δ .

C. Two-arms phase difference with double detunings

The rightmost panels of Figs. 3 and 4 report the phase difference between the sites of the two arms closest to the drain in the presence of two detunings. As in the case of single detuning, the phase difference oscillations are minima in amplitude for $\alpha = 1$ far from resonances. For $\alpha = 2$, we observe strong phase difference oscillations; evident oscillations are observed also for $\alpha = 3$. In all the cases analyzed so far, the phase difference oscillations follow in frequency those of populations. Also in this case, the phase oscillations are correlated to the ring population oscillations: the phase oscillation amplitude is bigger when the ring is more populated. However, a little amount of excitation in the ring is sufficient to have substantial oscillations in the phase.

In Appendix E, we also discuss the phase difference dynamics for different locations of the detunings. As expected, phase oscillations strongly depend on it; if the detunings are located in such a way that the excitation fractions follow the same paths on the two arms of the ring, the phase difference is zero for any Δ . This result can be achieved by putting two equal detunings in two diametrically opposite zones of the arms. Otherwise, if the resonance location in Δ is the same and the two paths are different, the dynamics differs with the one considered here, with specific features depending on the geometry.

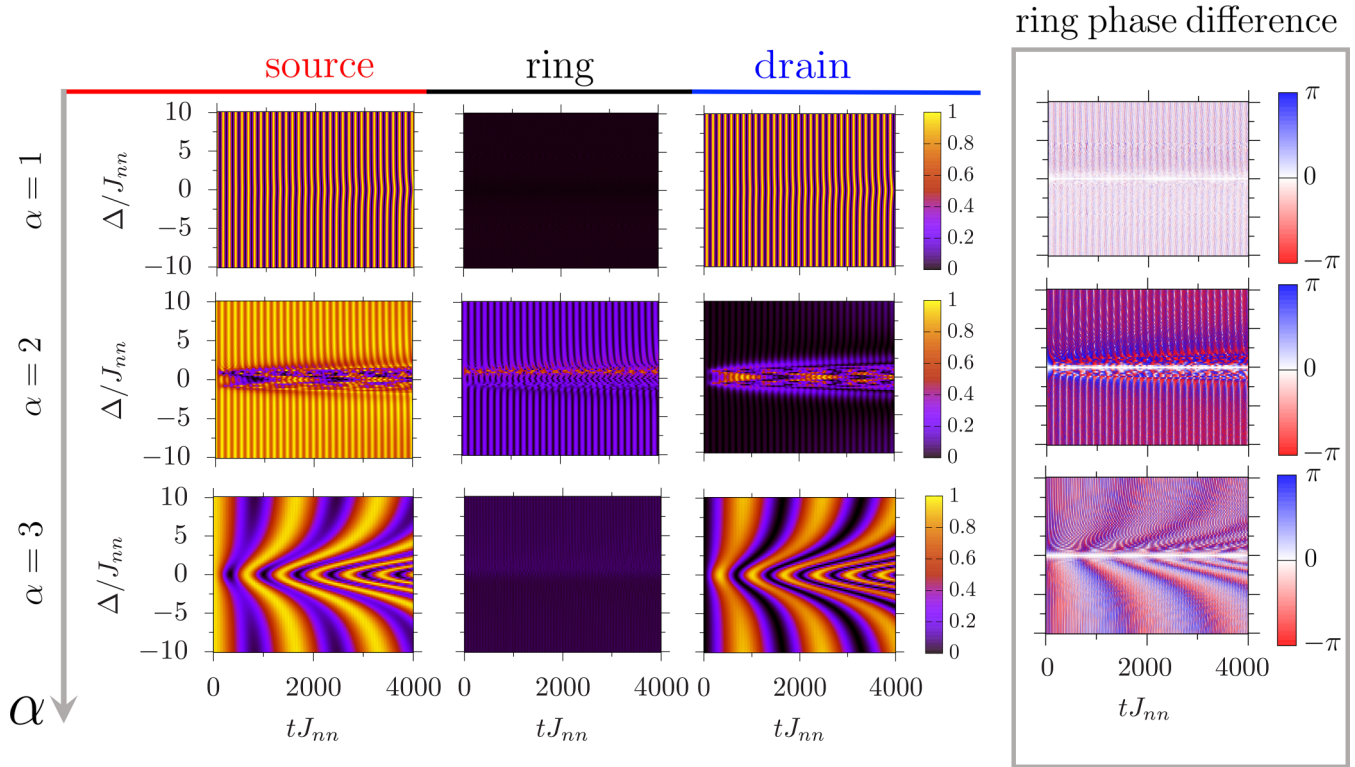


FIG. 4. Same as in Fig. 3, but for two detunings with equal magnitude but opposite sign: $\Delta_A = -\Delta_B = \Delta$.

V. DISCUSSION

We studied the source-drain excitation transport through a ring lattice track in which, in one or two sites, the atoms are detuned by Δ with respect to the others; such detunings act as local energy shifts in the system and therefore play the role of localized impurities. Motivated by the know-how in quantum technology, the system is described by a XY Hamiltonian with $1/d^\alpha$ hopping; specific values of α that are relevant for ion traps [25,35,54] and Rydberg atoms [26] localized in optical tweezers are considered. In the case of trapped ions, the hopping range is controllable through α which can be tuned in the $[0,3]$ interval, while for Rydberg atoms, $\alpha = 3$ is fixed by the dipole-dipole interaction. On the other hand, Rydberg atoms trapped in optical tweezers enjoy a huge freedom in the geometry in which they can be located, while the realization of traps with the desired geometry in ion systems is more challenging. The long-range nature of the hopping should be contrasted with previous studies corresponding to nearest-neighbor hopping in matter-wave systems [10]. The transport properties can be controlled by tuning Δ , with distinctive features depending on α .

The energy excitation is initialized in the source lead, with a zero-energy state. Then it is transferred to the ring by quenching the interaction with the rest of the system. In the weak leads-ring tunneling regime, once the excitations are transferred to the ring track, they propagate within the ring with a fast time dynamics. The presence of localized detunings causes a shift of the energy levels of the XY Hamiltonian of the ring and, for specific values of Δ , a state resonant with the source one can occur. Inspired by rf- and dc-SQUIDs, we addressed the two cases of one and two detunings; in turn,

we considered two detunings with the same or with opposite sign. The number of detunings, their sign, and their locations strongly affect the nature of the transport. Indeed, as reported in Appendix B, the shift of the ring energy levels strongly depends on the features of the local detunings. Their number and locations, together with the hopping range, can be tuned to control the values of detuning for which the transport is resonant. Far from resonance, the dynamics is not affected by detuning configurations for $\alpha = 1$, while it is for $\alpha = 3$. In the first case, long-range hopping processes are relevant, localized detunings can be bypassed during the dynamics, and the system does not show dependence on their location. In the second case, nearest-neighbor hopping processes are still dominant and the dynamics strongly depends on detuning values in broad regions around resonances. The far-from-resonance dynamics depends on detuning configurations. The case $\alpha = 2$ shows an intermediate behavior: while far from resonance the dynamics does not depend on the detuning configurations, close to resonance it is detuning dependent in a broad region. Overall, resonant and nonresonant transport display distinctive features. For resonant transport, the excitation can be transferred from the source to drain, while the ring track is moderately occupied. Far from resonance, the excitation oscillates between source and drain, minimally populating the ring on the observed timescales. The nature of the oscillation depends on the characteristics of the ring. Clearly, the far-off-resonance dynamics is nearly independent of the detuning (indicating that the detuned sites are bypassed by the long-range hopping). By increasing α , we observe a nontrivial effect of detunings, which is first localized around the resonant transport and then extended to the nonresonant dynamics. In Appendix D 3, we analyzed the effects of possible noise in the

detunings for $\alpha = 3$. A small noise does not affect the spectral structure and is expected to not alter the general features of the dynamics. In contrast, a noise comparable with Δ alters the structure of the spectrum and may cause uncontrollability of transport.

By studying the phase difference between upper and lower arms of the ring, we can conclude that the detuning can affect the phase of excitations (similarly to the effect of barriers in matter-wave propagation). The corresponding phase difference is observed to oscillate, even for small population oscillations. Phase difference and population oscillation frequencies are related.

Besides its own interest, our work may constitute the starting point to conceive devices of practical value employing Rydberg atoms or trapped ions. The realization of quantum analogues of classical circuits components, in the wake of what has been proposed in Ref. [55], is a possible example in this direction, with the difference that here, the spectral and geometrical properties of the channel are used to control the transport. Moreover, since localized detunings are experimentally feasible and behave like potential barriers, these types of systems can constitute a possible platform for the realization of analogues of a SQUID, in which the flow occurs in terms of excitations, rather than of matter. In addition, the control of the excitation dynamics in spin models may turn out to be useful for quantum batteries [56]; in particular, the possibility to tune the hopping between two two-level systems, being source and drain in this case, can be used to control charging and storing processes [57]. Finally, we point out that our logic can be feasibly extended to systems with different geometries, also in the presence of noise.

ACKNOWLEDGMENTS

We thank Giampiero Marchegiani and Tobias Haug for useful discussions. The Julian Schwinger Foundation Grant No. JSF-18-12-0011 is acknowledged. O.M. also acknowledges support by the H2020 ITN ‘‘MOQS’’ (Grant Agreement No. 955479) and MUR (Ministero dell’Universita e della Ricerca) through the PNRR MUR Project No. PE0000023-NQSTI.

APPENDIX A: DISTANCE AND WEAK-COUPPLING LIMIT

Here we provide a proper definition of the intraring and ring-leads distances; then we specify what we mean for weak ring-leads coupling. To define the distances, we first introduce an appropriate labeling of the atoms in the ring: supposing to work with an even number of sites in the ring, we label as N_r the site closest to the source and $N_r/2$ the site closest to the drain. We identify with $\varphi_j = 2\pi j/N_r$ the angle associated to site j of the ring. Given this labeling, the source-ring distance is

$$d_{S,j} = \sqrt{(d_{S,\mathcal{R}} + R)^2 + R^2 - 2(d_{S,\mathcal{R}} + R)R \cos \varphi_j}, \quad (\text{A1a})$$

where R is the radius of the ring and $d_{S,\mathcal{R}}$ is the distance between the source and the site N_r . Analogously, the drain-

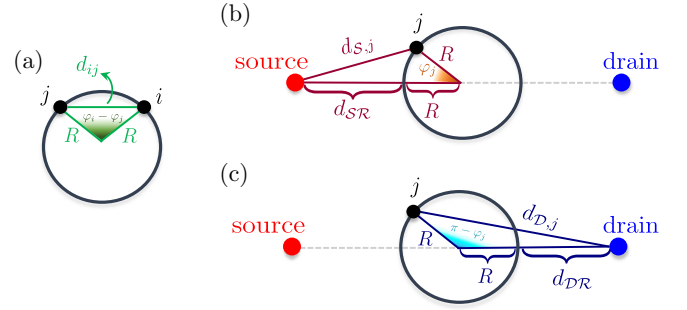


FIG. 5. Pictorial representation of distances in the system considered. (a) Intraring distance between two sites located at positions i and j . (b) Source-ring distance. (c) Drain-ring distance.

ring distance is

$$d_{D,j} = \sqrt{(d_{D,\mathcal{R}} + R)^2 + R^2 - 2(d_{D,\mathcal{R}} + R)R \cos(\pi - \varphi_j)}, \quad (\text{A1b})$$

with $d_{D,\mathcal{R}}$ the distance between the drain and the site $N_r/2$. In both cases, $j = 1, \dots, N_r$. The intraring distance is

$$d_{i,j} = 2R \sin\left(\frac{|\varphi_i - \varphi_j|}{2}\right) = 2R \sin\left(\frac{\pi|i - j|}{N_r}\right), \quad (\text{A1c})$$

where $i, j = 1, \dots, N_r$. Finally, the source-drain distance is $d_{S,D} = d_{S,\mathcal{R}} + 2R + d_{D,\mathcal{R}}$. A sketch of the distances is reported in Fig. 5.

Given a proper definition of the intraring and leads-ring distances, we introduce the intraring nearest-neighbor (nn) hopping,

$$J_{nn} = \frac{g}{d_{nn}^\alpha} \quad \text{with} \quad d_{nn} = 2R \sin\left(\frac{\pi}{N_r}\right), \quad (\text{A2})$$

and the leads-ring nearest-neighbor hopping,

$$K_{nn} = \frac{g}{d_{S,\mathcal{R}}^\alpha} = \frac{g}{d_{D,\mathcal{R}}^\alpha}, \quad (\text{A3})$$

where we are assuming $d_{S,\mathcal{R}} = d_{D,\mathcal{R}}$. In the main text, we work in the weak leads-ring coupling limit $K_{nn} \ll J_{nn}$, meaning $d_{S,\mathcal{R}}^\alpha \gg d_{nn}^\alpha$. Thus, if we consider $K_{nn} = J_{nn}/M$, with M an integer bigger than one, the distances will be related by $d_{S,\mathcal{R}} = M^{1/\alpha} d_{nn}$.

APPENDIX B: RING SPECTRAL ANALYSIS

In the weak-coupling regime, the ring and leads modes can be treated separately; their relation is crucial to understand the nature of the transport. The initial state of our protocol is a zero-energy state, and thus the presence of zero-energy modes in the ring is responsible for the population of the latter during the dynamics. In the absence of zero-energy modes in the ring, the latter will not be populated and the dynamics will result in coherent oscillations between source and drain. In this section, we will study the effect of localized detunings on the spectrum of an XY model in a ring. We first use a perturbative approach to study the effect of the detunings on the spectrum of the nearest-neighbor model; it is instructive to understand the possible presence of resonances between ring and drain. Then, we numerically analyze the modification of the ring

Hamiltonian spectrum due to the long-range hopping, paying particular attention to the changes in terms of resonances with zero-energy modes. We work in the one-excitation sector of the Hamiltonian.

1. Nearest-neighbor XY energy shift due to detuning

Let us consider the generic Hamiltonian

$$\hat{\mathcal{H}} = \hat{\mathcal{H}}_0 + \lambda \hat{\mathcal{H}}', \quad (\text{B1})$$

where $\hat{\mathcal{H}}_0$ is the unperturbed Hamiltonian, while $\hat{\mathcal{H}}'$ is a perturbation whose intensity λ is supposed to be small with respect to the unperturbed eigenvalues. We consider a Hamiltonian that possesses at least a couple of degenerate states $|E_a^0\rangle$ and $|E_b^0\rangle$ such that

$$\hat{\mathcal{H}}_0 |E_{a,b}^0\rangle = E^{(0)} |E_{a,b}^0\rangle \quad (\text{B2})$$

and work in the subspace spanned by these two states. Let us introduce the matrix element

$$W_{ij} = \langle E_i^0 | \hat{\mathcal{H}}' | E_j^0 \rangle. \quad (\text{B3})$$

The first-order correction to the unperturbed eigenvalue is [19]

$$E_{\pm}^{(1)} = \frac{1}{2} [W_{aa} + W_{bb} \pm \sqrt{(W_{aa} - W_{bb})^2 + 4|W_{ab}|^2}],$$

$$E_{\pm} = E^{(0)} + \lambda E_{\pm}^{(1)}. \quad (\text{B4})$$

Now, we consider an XY model on a ring composed of N_r sites perturbed by a localized detuning term,

$$\hat{\mathcal{H}} = J \sum_{j=1}^{N_r} (\hat{\sigma}_j^+ \hat{\sigma}_{j+1}^- + \text{H. c.}) + \Delta \sum_{j=1}^{N_r} \hat{n}_j \delta_{j,j_0} = \hat{\mathcal{H}}_0 + \Delta \hat{\mathcal{H}}', \quad (\text{B5})$$

where Δ is the perturbative parameter and we work in the one-excitation sector. The unperturbed Hamiltonian can be diagonalized by transforming the spins in fermions via a Jordan-Wigner transformation [58,59],

$$\hat{c}_j = \left(\prod_{\ell < j} \hat{\sigma}_{\ell}^z \right) \hat{\sigma}_j^-, \quad (\text{B6})$$

such that the $\hat{c}_j^{(\dagger)}$ operators obey the usual anticommutation relations for fermions. The resulting unperturbed model is a fermionic nondiagonal Hamiltonian. In the one-excitation sector, the fermionic operators are rotated through the transformation,

$$\hat{c}_j^{\dagger} = \frac{1}{\sqrt{N_r}} \sum_{n=1}^{N_r} e^{2\pi i j n / N_r} \hat{d}_n^{\dagger}, \quad (\text{B7})$$

and the diagonal unperturbed Hamiltonian is obtained [59,60],

$$\hat{\mathcal{H}}_0 = \sum_{n=1}^{N_r} E_n^{(0)} \hat{d}_n^{\dagger} \hat{d}_n, \quad E_n^{(0)} = 2J \cos\left(\frac{2\pi n}{N_r}\right). \quad (\text{B8})$$

Defining the momentum $k = 2\pi n / N_r$, we can observe that the eigenvalues of the Hamiltonian are all doubly degenerate, except for the ground state and the maximum excited state. We can easily observe that the couples of degenerate eigenstates are of the form $|k\rangle$ and $|2\pi - k\rangle$ (or, alternatively, $|n\rangle$ and $|N_r - n\rangle$), which refers to states with momenta k and $2\pi - k$;

thus we can restrict our analysis in the subspace spanned by these two states. Here, the perturbation matrix element is

$$W_{k,k'} = \langle k | \hat{n}_{j_0} | k' \rangle. \quad (\text{B9})$$

To perform the computation, it is convenient to transform the number operator in terms of Jordan-Wigner fermions in the momentum space. After that, the first matrix element to which we are interested is

$$W_{k,k} = \frac{1}{N_r} \sum_{m,m'=1}^{N_r} e^{-2\pi i m j_0 / N_r} e^{2\pi i m' j_0 / N_r} \langle n | \hat{d}_m^{\dagger} \hat{d}_{m'} | n \rangle$$

$$= \frac{1}{N_r} \sum_{m,m'=1}^{N_r} e^{2\pi i (m' - m) j_0 / N_r} \delta_{n,m} \delta_{m',n} = \frac{1}{N_r}$$

$$= W_{2\pi - k, 2\pi - k}. \quad (\text{B10})$$

At the same time, the off-diagonal term will be

$$W_{k, 2\pi - k} = \frac{1}{N_r} \sum_{m,m'=1}^{N_r} e^{2\pi i (m' - m) j_0 / N_r} \delta_{n,m} \delta_{m', N_r - n}$$

$$= \frac{e^{2ik j_0}}{N_r} = W_{2\pi - k, k}^*. \quad (\text{B11})$$

Given the perturbation matrix elements, we can compute the first-order energy corrections using Eq. (B4),

$$E_{\pm} = E^{(0)} + \Delta \frac{2 \pm 2}{2N_r}. \quad (\text{B12})$$

Thus, one of the two degenerate states remains unchanged and the other one is shifted by a factor $2\Delta / N_r$. The nondegenerate eigenvalues E_{GS} and E_{\max} are shifted by a common factor $W_{k_{GS}, k_{GS}} = \langle k_{GS} | \hat{n}_{j_0} | k_{GS} \rangle = W_{k_{\max}, k_{\max}} = \langle k_{\max} | \hat{n}_{j_0} | k_{\max} \rangle = \Delta / N_r$, where k_{GS} and k_{\max} are the momenta associated, respectively, to the ground and the maximum energy state.

In the case of two detunings with the same sign, the perturbation Hamiltonian is

$$\hat{\mathcal{H}}' = \hat{n}_{j_A} + \hat{n}_{j_B}; \quad (\text{B13})$$

the perturbation matrix elements are

$$W_{k,k} = \frac{2}{N_r} = W_{2\pi - k, 2\pi - k}, \quad (\text{B14a})$$

$$W_{k, 2\pi - k} = \frac{1}{N_r} (e^{2ik j_A} + e^{2ik j_B}) = W_{2\pi - k, k}^*. \quad (\text{B14b})$$

Given the matrix elements, we can compute the energy correction for degenerate states via

$$(B4)E_{\pm} = E^{(0)} + \frac{\Delta}{N_r} \{2 \pm \sqrt{2 + 2 \cos[2k(j_A - j_B)]}\}. \quad (\text{B15})$$

If we set the barriers in opposite sides of the ring, i.e., $j_A = [N_r/4]$ and $j_B = [3N_r/4]$, in such a way that $|j_A - j_B| = N_r/2$, we obtain a shift of a factor 0 or $4\Delta / N_r$ for each state. On the other hand, the ground and the maximum energy states are both shifted by a factor $2\Delta / N_r$.

Finally, it is straightforward to observe that the first-order correction to the energy states in the presence of two barriers with opposite sign gives zero contribution at the first perturbative order. To do that, it is sufficient to perform the same

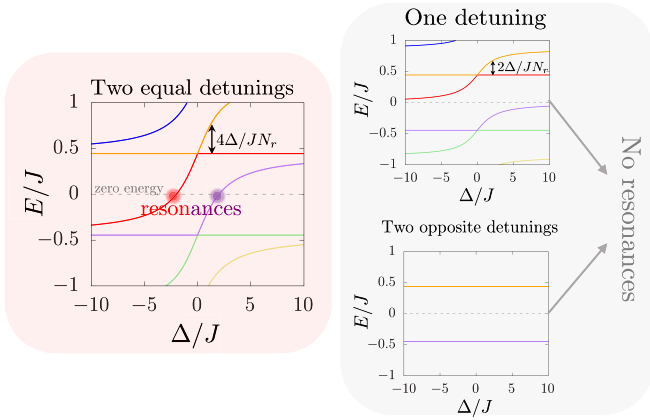


FIG. 6. Numerical results for the spectrum of the nearest-neighbor XY model in the presence of localized barriers. Only energies with energy near to zero are reported. The number of sites is $N_r = 14$.

calculation done for two equal detunings with $\hat{\mathcal{H}}' = \hat{n}_{j_A} - \hat{n}_{j_B}$. If $|j_A - j_B| = N_r/2$, the first-order energy correction is zero for each state of the spectrum.

Figure 6 reports the numerical results for the energy shifts in the presence of localized detunings. Through the numerical computation, we easily understand what happens beyond the first perturbative order. In particular, for both single and double equal detunings, the first-order shifts in Δ are corrected for big values of the latter tending to flatten. The main difference between the two cases is the slope of the shift at small values of the detuning. The one of the single-barrier case is smaller than the one of the double-barrier case. Thus, while in the latter it is sufficient to permit to two levels to cross the zero-energy mode, in the single-barrier case of the linear shift, it is not sufficient. It is important to observe that we do not observe resonances in our Δ range; it is possible that they are present for bigger values of the detuning. However, in the case of two opposite detunings, the reported degenerate states are not shifted even for more than first-order contributions; then, we do not expect resonances, and the dynamics is characterized by coherent oscillations between source and drain.

2. Long-range XY energy shift due to detuning

For a nearest-neighbor XY model, the spectrum is symmetric with respect to the zero-energy states, meaning that the energies are organized in pairs, $\pm E_n$. We also showed how from the energy shifts we expect that the resonances

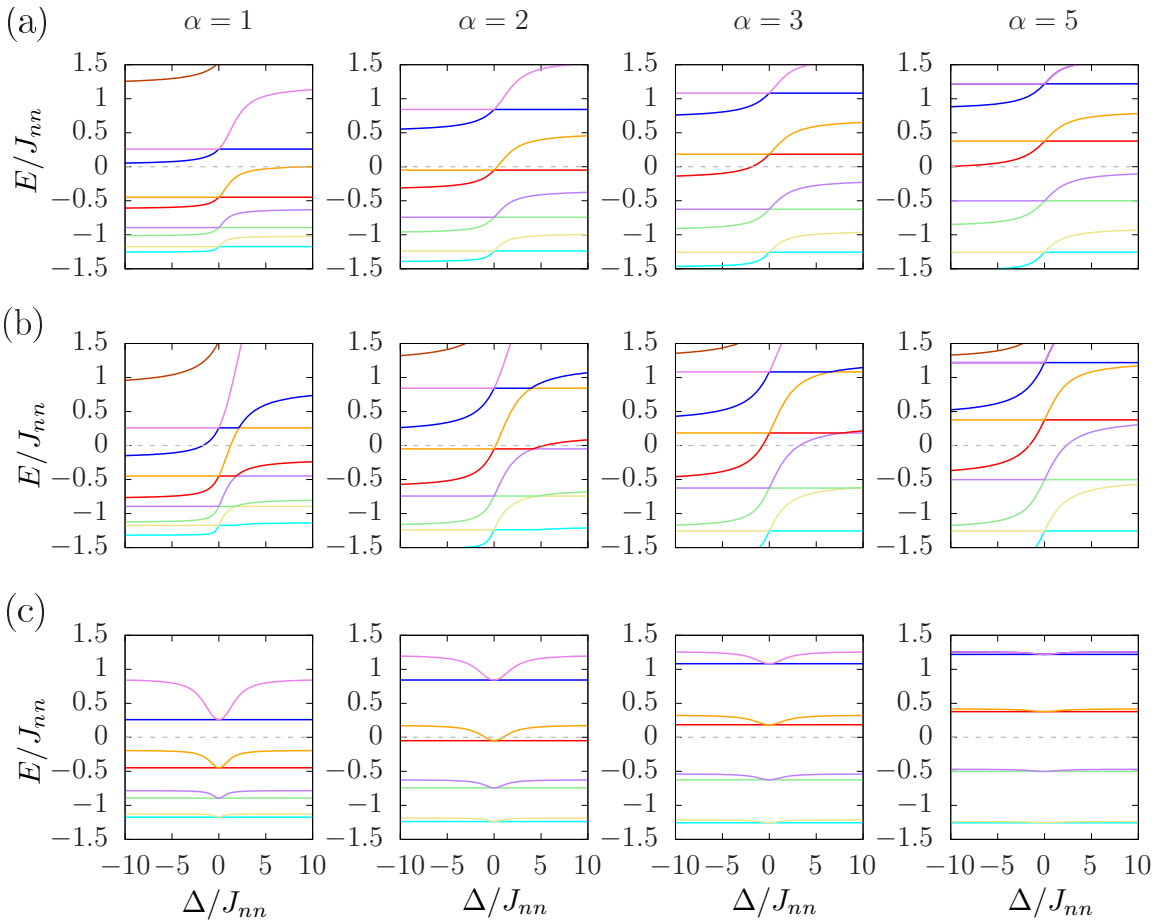


FIG. 7. Numerical results for the spectrum of the long-range XY model in the ring in the presence of localized detunings (2a). Only close-to-zero energies are reported. The plot is organized in three panels: (a) Results in the presence of a single detuning, (b) results in the presence of two equal detunings, and (c) results in the presence of two opposite detunings. For each panel, we show results for $\alpha = 1, 2, 3, 5$. The number of sites is $N_r = 14$.

are symmetric for $\Delta \rightarrow -\Delta$. However, the dynamics reported in the main text shows that for long-range hopping, this is not true. The ring population does not follow a symmetric behavior with respect to $\Delta = 0$. Therefore, a detailed analysis of the energy shift in the spectrum is important to understand the asymmetry in the dynamics. The model with which we work here is (2a).

Figure 7 reports the energy spectrum in all three paradigmatic detuning configurations considered so far. Before analyzing the effect of the detuning, it is necessary to pay attention to the role of the inverse hopping range α for $\Delta = 0$. We can immediately observe that for each value of α , the degeneracies persist; on the other hand, a substantial shift of the levels is observed. Passing from $\alpha = 5$ to $\alpha = 1$, the levels lose their symmetry with respect to $E = 0$ and tend to crush to a negative-energy value. This means that the first $E > 0$ and the first $E < 0$ states no longer possess symmetric energy with respect to zero. When the detuning is switched on, the energy levels are shifted and cross the zero-energy mode.

To be more quantitative, let us first consider the case of the single barrier reported in Fig. 7(a). Here, the levels that cause resonances are the orange and red. Increasing the hopping range, the red and the orange levels are shifted downwards; during the shift, one of the two levels crosses the zero-energy mode, giving rise to one resonance at negative Δ . The purple level in the nearest-neighbor limit is not sufficiently shifted to give rise to a positive resonance at positive Δ in the interval considered so far. Then, for one detuning, we have only one value or narrow range of Δ for which the ring becomes populated during the dynamics.

Figure 7(b) reports the results for two equal detunings: for each value of α , there are at least two values of Δ for which the zero-energy mode is crossed, as in the nearest-neighbor case. In the presence of two opposite detunings [Fig. 7(c)], the long-range hopping is responsible for a shift of the energy levels that is quadratic in the detuning Δ . As in the nearest-neighbor limit, also in the presence of long-range hopping, the first-order correction is zero, and thus the shift scales as Δ^2 with a coefficient that increases as α decreases. For this reason, it is possible to have symmetric resonances with respect to $\Delta = 0$. In particular, in the reported plots, resonances appear at $\alpha = 2$.

It is safe to assume that the presence of the resonances also strongly depends on the number of atoms in the ring. The presence of size-dependent resonance location can be immediately deduced from the perturbative results obtained in the previous section. Indeed, the unperturbed energy is $E_k^{(0)} = 2J \cos k$, where $k \sim 1/N_r$ and the first-order shifts are directly proportional to Δ/N_r . In the presence of long-range hoppings, we do not have access to the exact spectrum of the Hamiltonian; however, at least for a finite value of N_r , we can analyze how the resonance position moves, increasing the size. To be more precise, we consider the case of a single barrier and plot the crossing states as a function of Δ . Here, for crossing states, we mean the states that cross the zero-energy level in the interval $\Delta \in [-10, 0]$.

Figure 8 reports them and the first-order linear corrections $E^{(0)} + 2\Delta/N_r$, where we extracted $E^{(0)}$ from numerical data and assumed that the first-order perturbative shift is unchanged with respect to the nearest-neighbor case. We immediately observe that for small values of Δ , the linear shift

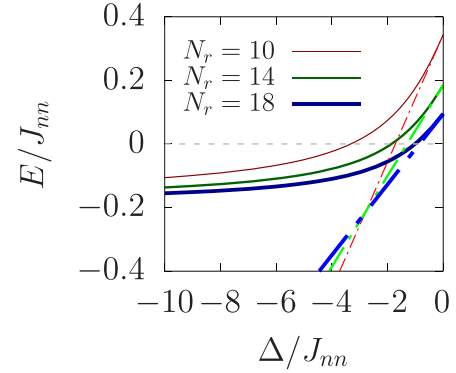


FIG. 8. Crossing energy states in the presence of a single barrier located at $j_0 = \lceil N_r/4 \rceil$ for three different values of the number of atoms in the ring, N_r . The solid lines refer to numerical values of the energy for $N_r = 10$ (dark red), $N_r = 14$ (dark green), and $N_r = 18$ (dark blue); the thickness of the curves is in descending order in the size N . The dashed red, green, and blue lines refer to first perturbative order corrections $E^{(0)}/J_{nn} + 2\Delta/J_{nn}N_r$ for, respectively, $N_r = 10, 14, 18$. In all three cases, $\alpha = 3$.

keeps working well; indeed, increasing the size of the system, the slope of the shift is smaller. Moreover, the energy $E^{(0)}$ is smaller, increasing the size, and this makes the resonance position located at smaller values of $|\Delta|$ for bigger values of the size. Finally, we observe that already for $N_r = 18$, the position of the resonance can be qualitatively estimated from the linear shift as $\Delta_{\text{res}} \approx -E^{(0)}N_r/2$ since it is located at a relatively small value of the detuning.

APPENDIX C: DYNAMICS IN ABSENCE OF DETUNINGS

Here we analyze the dynamics of the system in the absence of any type of detuning. We expect to find a nontrivial dynamics also in the absence of it; due to the geometry of the system, the excitation that travels along the system is subject to many scattering and splitting events. To have an idea of the complexity of the dynamics, let us consider an excitation subject only to nearest-neighbor hopping that travels in the system starting from the source. The excitation moves from the source to the nearest site on the ring. The coupling between source and ring is smaller compared to the intraring one; thus, once a small excitation fraction reaches the ring, it is quickly split in the two arms of the ring. The split excitation fractions travel in the two arms of the ring and meet at the end of them, before the drain. Here, they scatter, a part of the excitation hops to the drain, and the rest continue their dynamics in the arms of the ring. During a long time evolution, a lot of scattering events occur and the dynamics will be complex and not intuitively easy to describe.

Figure 9 reports the population dynamics of the drain for different values of the inverse hopping range α . We consider $\alpha = 1$, $\alpha = 3$, nearest-neighbor limit, and the particular value of α for which, in the absence of detuning, the ring presents zero-energy levels resonant with the initial state. For instance, from Fig. 7 we can observe that for $N = 16$, the particular α_{res} value is close to 2. Indeed, we find $\alpha_{\text{res}} = 2.168$; the other α_{res} values are reported in the Fig. 9 caption. We observe how the drain population oscillates quite regularly except in the

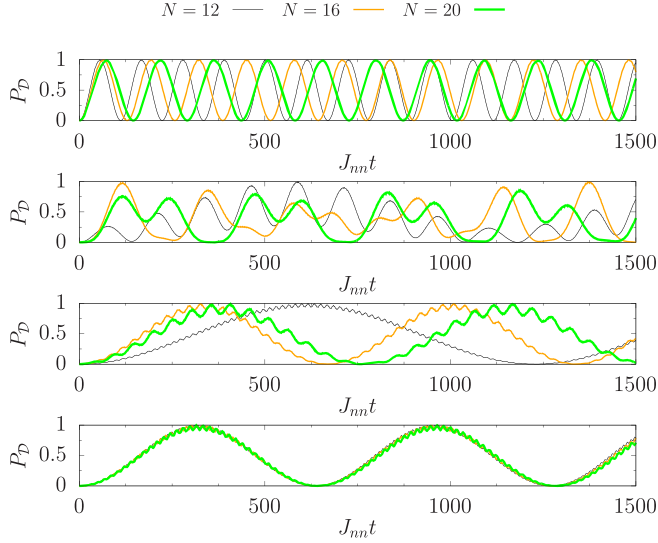


FIG. 9. Dynamics of the drain population in the absence of detunings in the ring. Results are reported for three different values of the size of the system: $N = 12$ (orange), $N = 16$ (green), and $N = 20$ (black); the thickness of the curves is in ascending order in the size N . The four panels refer to different values of the inverse hopping range: (a) $\alpha = 1$, (c) $\alpha = 3$, and (d) nearest neighbor. (b) The dynamics for the values of the inverse hopping range for which the ring presents zero-energy levels in the absence of detunings. These values are $\alpha_{\text{res}} = 1.731$ ($N = 12$), $\alpha_{\text{res}} = 2.168$ ($N = 16$), $\alpha_{\text{res}} = 2.508$ ($N = 20$). Leads and ring are weakly coupled, $K_{nn}/J_{nn} = 0.1$.

α_{res} case; the ring is well populated and the oscillations are extremely irregular. For the other cases, the ring is weakly populated (see Figs. 2–4), and thus it is important to follow the behavior of the drain density.

The latter is characterized by small frequency oscillations with big amplitude modulated by fast oscillations with small amplitude. In the nearest-neighbor limit, the two frequencies can be evaluated analytically [10],

$$\begin{aligned} \frac{\omega_{\pm}}{J_{nn}} = & \pm \frac{N_r}{\delta} \frac{8 + \tilde{K}_{nn}^2 N_r - 2\tilde{K}_{nn}^2 \delta}{4\tilde{K}_{nn}^2 \delta^2 - N_r(8 + \tilde{K}_{nn}^2 N_r)} \\ & + \left\{ \left(\frac{N_r}{\delta} \frac{8 + \tilde{K}_{nn}^2 N_r - 2\tilde{K}_{nn}^2 \delta}{4\tilde{K}_{nn}^2 \delta^2 - N_r(8 + \tilde{K}_{nn}^2 N_r)} \right)^2 \right. \\ & \left. + \frac{N_r}{\delta} \frac{8\tilde{K}_{nn}^2}{8N_r + \tilde{K}_{nn}^2(N_r^2 - 4\delta^2)} \right\}^{1/2}, \quad (\text{C1}) \end{aligned}$$

where $\tilde{K}_{nn} = K_{nn}/J_{nn}$ and $\delta = \csc(\pi/N_r)$. From the numerical computation, we can observe that the frequencies are weakly dependent on the size of the system. The nontrivial form of the frequencies confirms how the dynamics is complex.

Surprisingly, for $\alpha = 3$, the dynamics changes a lot with respect to the nearest-neighbor limit. One of the crucial differences is that here the leads are strongly connected to a plethora of sites near to the N_r and $N_r/2$, not just with one site. The first counterintuitive result is the slow down of the dynamics with respect to the nearest-neighbor case. The presence of hoppings does not cause a faster transport of the excitation from one site to the other. Second, the transport is slower for

$N = 12$, while $N = 16$ is the faster case. Thus, a smaller size does not correspond to faster dynamics. Last, the case $\alpha = 1$ is the most intuitive one. The hopping range is sufficiently large to avoid complex internal effects in the ring. The oscillations are faster with respect to all the other cases considered with a smaller hopping range; moreover, increasing the system size, it becomes slower.

APPENDIX D: INFORMATION ON THE DYNAMICS FROM THE COMPLETE SPECTRUM

In Appendix B, we showed that important information on the dynamics can be extracted from the bare ring Hamiltonian, assuming that the ring and the leads are weakly coupled. Here, we focus our attention on the complete Hamiltonian, describing how the resonances manifest themselves on the state population and how the transport nature is modified and damaged from strong coupling and disorder.

1. Full Hamiltonian eigenstate nature

In the one-excitation sector, a generic eigenstate of the Hamiltonian can be written in the computational basis as

$$|E_n\rangle = c_S^{(n)} |S\rangle + |\mathcal{R}\rangle + c_D^{(n)} |D\rangle, \quad (\text{D1})$$

where $|\mathcal{S}\rangle = |\uparrow\rangle_S \otimes |\downarrow, \dots, \downarrow\rangle_{\mathcal{R}} \otimes |\downarrow\rangle_{\mathcal{D}}$, $|\mathcal{R}\rangle = \sum_{j \in \mathcal{R}} c_j^{(n)} |\downarrow\rangle_S \otimes |\downarrow, \dots, \uparrow_j, \dots, \downarrow\rangle_{\mathcal{R}} \otimes |\downarrow\rangle_{\mathcal{D}}$, and $|\mathcal{D}\rangle = |\downarrow\rangle_S \otimes |\downarrow, \dots, \downarrow\rangle_{\mathcal{R}} \otimes |\uparrow\rangle_{\mathcal{D}}$ are, respectively, the source, ring, and drain states. In the absence of resonances, it is safe to assume that the leads and the ring degrees of freedom are separated. Thus, we group the states of the Hamiltonian in three classes: $\{|E_{n_l}\rangle, |E_{n_r}\rangle, |E_{n_{lr}}\rangle\}$, where $|E_{n_l}\rangle$ are states in which all the excitations are in the leads, $|E_{n_r}\rangle = |\mathcal{R}\rangle$ are states in which only the ring is populated, and $|E_{n_{lr}}\rangle$ are states in which the population is distributed between ring and leads. The labels satisfy the relation $n_l + n_r + n_{lr} = N$. Since the initial state of our protocol is $|\psi(0)\rangle = |S\rangle$ and $\langle \mathcal{R} | S \rangle = 0$, the states $|E_{n_r}\rangle$ will not contribute to the dynamics; thus, the generic time-evolved state can be written as

$$\begin{aligned} |\psi(t)\rangle = & \sum_{n_l} e^{-iE_{n_l}t} \langle E_{n_l} | S \rangle |E_{n_l}\rangle \\ & + \sum_{n_{lr}} e^{-iE_{n_{lr}}t} \langle E_{n_{lr}} | S \rangle |E_{n_{lr}}\rangle. \quad (\text{D2}) \end{aligned}$$

Moreover, if the Hamiltonian spectrum does not contain uniform states $|E_{n_{lr}}\rangle$, the dynamics is dominated by the leads states $|E_{n_l}\rangle = c_S^{(n_l)} |S\rangle + c_D^{(n_l)} |D\rangle$ and will result in oscillations between source and drain of the form

$$|\psi(t)\rangle = \sum_{n_l} e^{-iE_{n_l}t} [c_S^{(n_l)} |S\rangle + c_D^{(n_l)} |D\rangle]. \quad (\text{D3})$$

The value of the lead state energies and their coefficients is fundamental to have information on the source-drain oscillation frequency and amplitude. On the other hand, the ring becomes populated only when the Hamiltonian has $|E_{n_{lr}}\rangle$ states. Thus, we expect to observe states $|E_{n_{lr}}\rangle$ in the spectrum in correspondence to the resonances.

Here we focus our attention on the eigenstate population $P_j^{(n)} = \langle E_n | \hat{n}_j | E_n \rangle$; we compute it for the source, ring, and

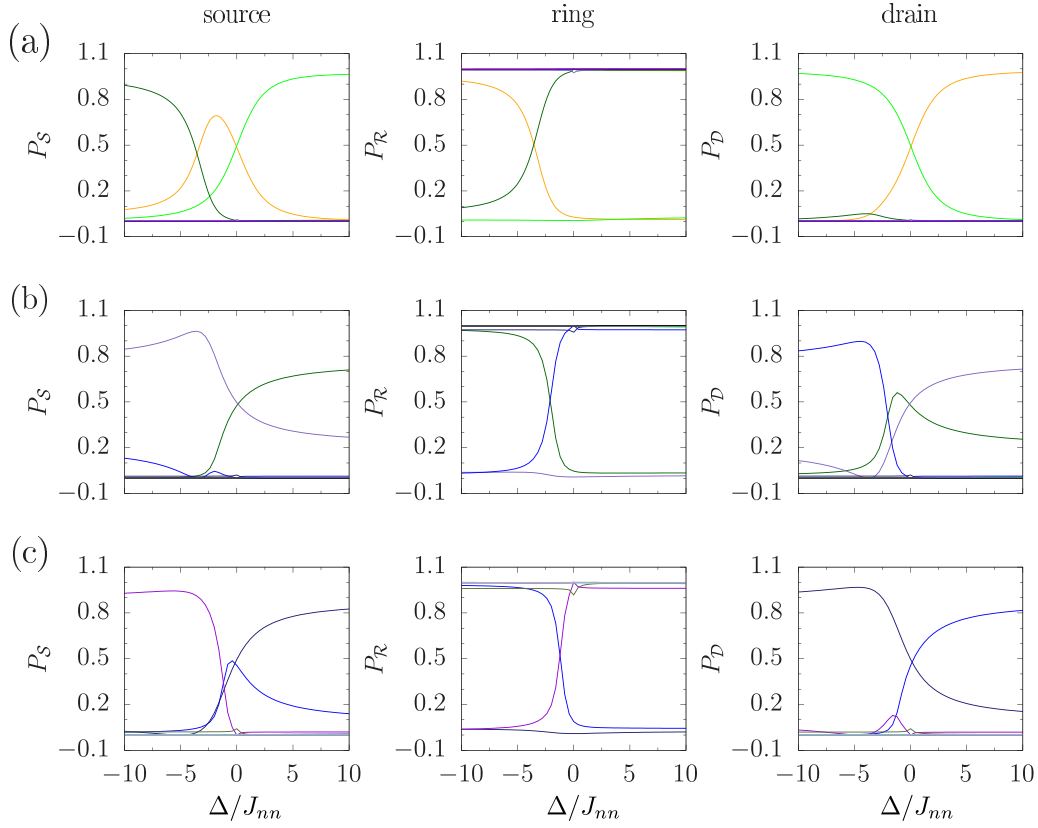


FIG. 10. Source, ring, and drain population, from left to right, in the spectrum for three different values of the size $N = N_r + 2$: (a) $N = 12$, (b) $N = 16$, and (c) $N = 20$. Most of the states are approximately ring states, meaning that their $P_{\mathcal{R}}^{(n)} \approx 1$. For each N , only three states are not ring states: for $N = 12$, the fifth, sixth, and seventh excited states; for $N = 16$, the seventh, eighth, and ninth excited states; for $N = 20$, the ninth, tenth, and 11th excited states. In all three plots, the parameters are set in such a way that $K_{nn}/J_{nn} = 0.1$, and $\alpha = 3$. Only one barrier is taken into account.

drain in the whole spectrum. Figure 10 reports the behavior of the eigenstate populations in the leads and ring for three different values of the size of the system; the inverse hopping range is $\alpha = 3$ and only one localized barrier at $j_0 = \lceil N_r/4 \rceil$ is taken into account. We immediately observe that the majority of the states of the system are ring states for which $P_{\mathcal{R}}^{(n)} \approx 1$ and $P_{S,D}^{(n)} \approx 0$; they do not contribute to the dynamics if the system is initialized in $|S\rangle$. Comparing between Figs. 8 and 10, we observe that in correspondence with the resonance, the ring population is 1/2 for two states of the spectrum, and the excitation is equally distributed between the ring and leads; this will result in a filling of the ring during the dynamics. Far from resonance, the Hamiltonian states are approximately ring or leads states with $P_{\mathcal{R}}^{(n)} \approx 0, 1$; thus, the dynamics will result in coherent oscillations between source and drain.

Let us observe that leads states possess $P_{\mathcal{L}}^{(n)} = P_S^{(n)} + P_D^{(n)} = 1$, and, therefore, the nature of the dynamics strongly depends on the source and drain population of the states. In particular, for $\Delta < \Delta_{\text{res}}$, there are source localized states, meaning states in which the source population is dominant above all the others. In the absence of uniform states, the dynamics follows Eq. (D3), which results in $|\psi(t)\rangle \approx e^{i\phi} |S\rangle$ if there is a dominant localized source state. Thus, for $\Delta < \Delta_{\text{res}}$, the excitation remains localized in the source or, at most, a

small fraction of it moves to the drain. The value of the population shows an irregular dependence on the size; the position of the resonance is size dependent and various finite-size effects come into play. Far from resonance, the size dependence is not regular, and the source and drain populations follow different behaviors without a well-defined dependence on the size. Thus, for each value of the size, there is a resonance, but the dynamics far from the resonance strongly depends on N .

2. Eigenstate leads population for different leads-ring coupling

In the previous section, we analyzed the full spectrum populations in the weak-coupling regime. Here, we go beyond it and study the system in terms of leads population. In particular, we analyze the leads magnetization that is directly related to leads and ring populations,

$$\hat{\sigma}_{\mathcal{L}}^z = \hat{\sigma}_S^z + \hat{\sigma}_D^z = 2(\hat{n}_{\mathcal{L}} - \hat{1}) = -2\hat{n}_{\mathcal{R}}. \quad (\text{D4})$$

This means that the leads and the ring states, respectively, have $\langle \hat{\sigma}_{\mathcal{L}}^z \rangle = 0$ and -2 .

We focus on the Rydberg case $\alpha = 3$. Figure 11 reports the leads magnetization for three different values of the leads-ring coupling. Increasing the coupling, the population of the eigenstates changes drastically. For small coupling, three states are

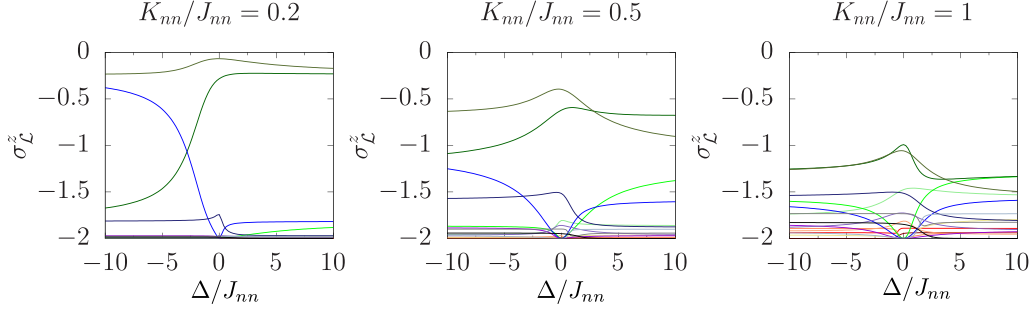


FIG. 11. Leads magnetization in the spectrum as a function of the barrier height Δ for different leads-ring couplings K_{nn}/J_{nn} . $N_r = 14$ and $\alpha = 3$ are considered. The ring contains a single barrier localized in $[N_r/4]$.

$|E_{n_r}\rangle$ states around the resonance point, they are the seventh, eighth, and ninth excited states. The others are approximately ring or leads states. Increasing K_{nn}/J_{nn} , both $|E_{n_r}\rangle$ and $|E_{n_l}\rangle$ states become $|E_{n_r}\rangle$ states. The spectrum is no longer separated in well-defined classes; this will result in a dynamics that is not characterized by coherent source-drain oscillation, but the ring will be populated not only for specific Δ values. Thus, the transport will no longer be controllable by tuning Δ .

3. Robustness against noise

Here we study the robustness of the results under the presence of disorder. In particular, we work with the impurity Hamiltonian

$$\hat{\mathcal{H}}_{\text{imp}} = \sum_{j \in \mathcal{R}} \Delta_j \hat{n}_j, \quad (\text{D5})$$

where Δ_j is randomly extracted in the interval $[-\epsilon, +\epsilon]$ for each j except for $j_0 = [N_r/4]$, in which Δ_j belongs to the interval $[\Delta - \epsilon, \Delta + \epsilon]$. Therefore, it corresponds to the case of the single localized barrier in the presence of noise. We study the effect of disorder on the leads population for $N_{\text{rea}} = 100$ disorder realizations in the single-barrier case for $N = 12$ and $\alpha = 3$. We report the behavior of the expectation value,

$$\overline{\langle E_n | \hat{\sigma}_L^z | E_n \rangle} = \frac{1}{N_{\text{rea}}} \sum_{\beta=1}^{N_{\text{rea}}} \langle E_n^{(\beta)} | \hat{\sigma}_L^z | E_n^{(\beta)} \rangle, \quad (\text{D6})$$

which is the leads magnetization expectation value in the Hamiltonian spectrum averaged over many disorder realizations. $|E_n^{(\beta)}\rangle$ is the n th eigenstate of the Hamiltonian for the

β -th disorder realization. Figure 12 reports the behavior of the leads magnetization for different values of the disorder. We can observe how the presence of disorder can be dangerous for the population; indeed, for strong disorder ($\epsilon = 1$), the ring and leads states can become $|E_{n_r}\rangle$ states. However, a little amount of disorder ($\epsilon = 0.1$) does not modify the structure of the populations. In the intermediate case $\epsilon = 0.5$, the population behavior is slightly modified but keeps well the zero disorder structure with a resonance and a well-defined separation between leads and ring states far from it.

APPENDIX E: PHASE DIFFERENCE DYNAMICS

Here we provide more details on the phase effects that the presence of localized detunings generate. In the first part, we show how the presence of a single localized detuning in the center of the chain of three atoms has significant effects on the phase associated to each site. For this reason, we suspect that a phase difference between two different paths with detuning located in different positions arises. In the second part of this Appendix and in the main text, we report the phase difference between two sites in the two arms in different conditions. We show that its dynamics is related to the population one.

1. Detuning-dependent phase difference in the three-sites system

The presence of a localized detuning introduces a time-dependent phase between different sites of the system. To see this, let us consider the simple three-sites problem. We suppose to consider only nearest-neighbor hopping and put a localized detuning in the middle of the chain. As a first

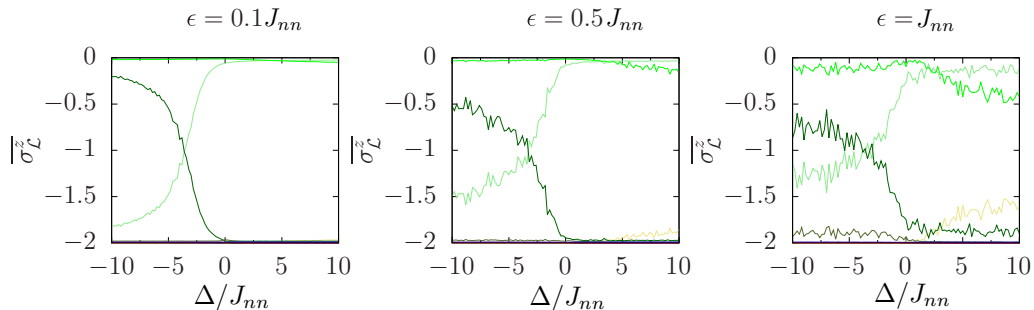


FIG. 12. Leads magnetization in the spectrum as a function of the barrier height Δ for different values of the disorder ϵ . We consider $K_{nn}/J_{nn} = 0.1$ (weak coupling). $N_r = 10$ and $\alpha = 3$ are considered. The impurity Hamiltonian is in Eq. (D5). The y axis reports the expectation value of $\hat{\sigma}_L^z$ for each n [see Eq. (D6)]. We average over $N_{\text{rea}} = 100$ disorder realizations.

stage, we fix the detuning $\Delta = 0$ and consider the three-site Hamiltonian

$$\hat{\mathcal{H}}_{\text{hop}} = J(\hat{\sigma}_1^+ \hat{\sigma}_2^- + \hat{\sigma}_2^+ \hat{\sigma}_3^- + \text{H.c.}). \quad (\text{E1})$$

$$|\psi(t)\rangle = \frac{1}{2}[\cos(\sqrt{2}Jt) + 1]|\uparrow_1, \downarrow_2, \downarrow_3\rangle + \frac{i}{\sqrt{2}}\sin(\sqrt{2}Jt)|\downarrow_1, \uparrow_2, \downarrow_3\rangle + \frac{1}{2}[\cos(\sqrt{2}Jt) - 1]|\downarrow_1, \downarrow_2, \uparrow_3\rangle; \quad (\text{E2})$$

in the absence of detuning, there is not a relative phase between the sites 1 and 3. In the presence of a localized detuning, the Hamiltonian considered is $\hat{\mathcal{H}} = \hat{\mathcal{H}}_{\text{hop}} + \Delta\hat{n}_2$, and the resulting time-evolved state is

$$\begin{aligned} |\psi(t)\rangle = & \left(\frac{e^{-i[\Delta-f(\Delta,J)]t/2}}{\mathcal{N}_1^2} + \frac{e^{-i[\Delta+f(\Delta,J)]t/2}}{\mathcal{N}_2^2} + \frac{1}{2} \right) |\uparrow_1, \downarrow_2, \downarrow_3\rangle \\ & + \left(\frac{[\Delta-f(\Delta,J)]e^{-i[\Delta-f(\Delta,J)]t/2}}{2J\mathcal{N}_1^2} + \frac{[\Delta+f(\Delta,J)]e^{-i[\Delta+f(\Delta,J)]t/2}}{2J\mathcal{N}_2^2} \right) |\downarrow_1, \uparrow_2, \downarrow_3\rangle \\ & + \left(\frac{e^{-i[\Delta-f(\Delta,J)]t/2}}{\mathcal{N}_1^2} + \frac{e^{-i[\Delta+f(\Delta,J)]t/2}}{\mathcal{N}_2^2} - \frac{1}{2} \right) |\downarrow_1, \downarrow_2, \uparrow_3\rangle, \end{aligned} \quad (\text{E3})$$

where $\mathcal{N}_1^2 = 2 + [\Delta - f(\Delta, J)]^2/4J^2$, $\mathcal{N}_2^2 = 2 + [\Delta + f(\Delta, J)]^2/4J^2$, and $f(\Delta, J) = \sqrt{\Delta^2 + 8J^2}$. In this way, the real and imaginary parts of the $|\uparrow_1, \downarrow_2, \downarrow_3\rangle$ state are

$$\text{Re}[c_{\uparrow\downarrow\downarrow}(t)] = \frac{\cos[(\Delta-f)t/2]}{\mathcal{N}_1^2} + \frac{\cos[(\Delta+f)t/2]}{\mathcal{N}_2^2} + \frac{1}{2}, \quad (\text{E4a})$$

$$\text{Im}[c_{\uparrow\downarrow\downarrow}(t)] = -\frac{\sin[(\Delta-f)t/2]}{\mathcal{N}_1^2} - \frac{\sin[(\Delta+f)t/2]}{\mathcal{N}_2^2}. \quad (\text{E4b})$$

The phase associated to the state is

$$\phi_{\uparrow\downarrow\downarrow}(t) = \tan^{-1} \left[\frac{\text{Im}[c_{\uparrow\downarrow\downarrow}(t)]}{\text{Re}[c_{\uparrow\downarrow\downarrow}(t)]} \right], \quad (\text{E5})$$

while the phase associated to the state $|\downarrow_1, \downarrow_2, \uparrow_3\rangle$ is

$$\phi_{\downarrow\downarrow\uparrow}(t) = \tan^{-1} \left[\frac{\text{Im}[c_{\downarrow\downarrow\uparrow}(t)]}{\text{Re}[c_{\downarrow\downarrow\uparrow}(t)] - 1} \right], \quad (\text{E6})$$

and, therefore, the two phases are different. In the presence of detuning, a nonzero relative phase between the first and the last sites of the chain is present. The difference with the zero-detuning case is clear: the states $|\uparrow, \downarrow, \downarrow\rangle$ and $|\downarrow, \downarrow, \uparrow\rangle$ acquire a Δ -dependent phase; also, the state $|\downarrow, \uparrow, \downarrow\rangle$ has a Δ -dependent phase, differently from the zero-detuning case in which it is fixed to $\pm\pi$.

2. Phase difference for different locations of detunings

If we consider two arms that differ from the detuning value, we expect to see a nontrivial phase difference between their sites. To formally evaluate the phase shift in the setup considered in the main text, we write the generic time-evolved states of the system in the position basis,

$$\begin{aligned} |\psi(t)\rangle = & c_S(t)|S\rangle \\ & + \sum_{j \in \mathcal{R}} c_j(t)|\downarrow\rangle_S \otimes |\downarrow, \dots, \uparrow_j, \dots, \downarrow\rangle_{\mathcal{R}} \otimes |\downarrow\rangle_D \\ & + c_D(t)|D\rangle, \end{aligned} \quad (\text{E7})$$

By considering the initial state $|\psi(0)\rangle = |\uparrow_1, \downarrow_2, \downarrow_3\rangle$ and evolve it through the Schrödinger equation, the resulting time-evolved state is

and we observe that the two-body correlator

$$\langle \hat{\sigma}_i^+ \hat{\sigma}_j^- \rangle = c_i^*(t)c_j(t) = |c_i(t)||c_j(t)|e^{i[\phi_j(t) - \phi_i(t)]} \quad (\text{E8})$$

is directly related to the phase shift. Thus, the phase difference between the two sites i and j is accessible through $\delta\phi(t) = \phi_j(t) - \phi_i(t) = \arg[\langle \hat{\sigma}_i^+ \hat{\sigma}_j^- \rangle]$. We can fix $i = N_r/2 - 1$ and $j = N_r/2 + 1$ in order to have information on the difference between the phases accumulated by excitation fractions crossing the two arms of the ring. Figures 2–4 report the phase difference dynamics and detuning dependence for the configurations in Fig. 1, displaying its relation with the population dynamics. Here, we show the phase difference for alternative choices of the detunings location in the Rydberg case $\alpha = 3$.

We immediately observe that when the two detunings have the same sign and their locations are symmetric with respect to the leads [Fig. 13(a)], the phase difference is zero everywhere.

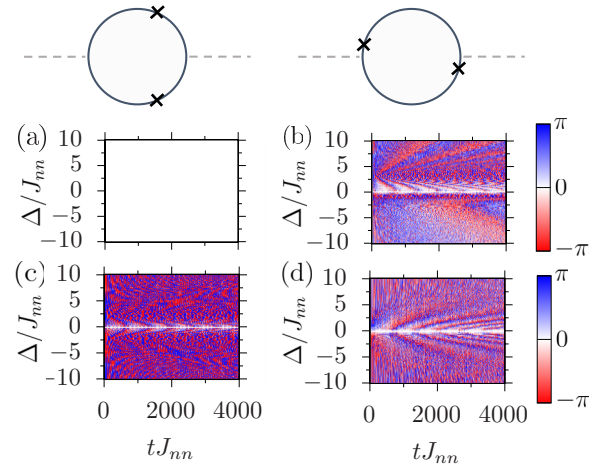


FIG. 13. Phase difference $\delta\phi$ as a function of detuning and time. (a),(c) Phase difference for two (a) equal and (c) opposite detunings located at $j_A = \lceil N_r/4 \rceil$ and $j_B = \lceil 3N_r/4 \rceil - 1$ as in the top-left sketch. (b),(d) Phase difference for two (b) equal and (d) opposite detunings located at $j_A = 1$ and $j_B = N_r/2 + 1$ as in the top-right sketch. The hopping range is fixed to $\alpha = 3$, $K_m/J_m = 0.1$

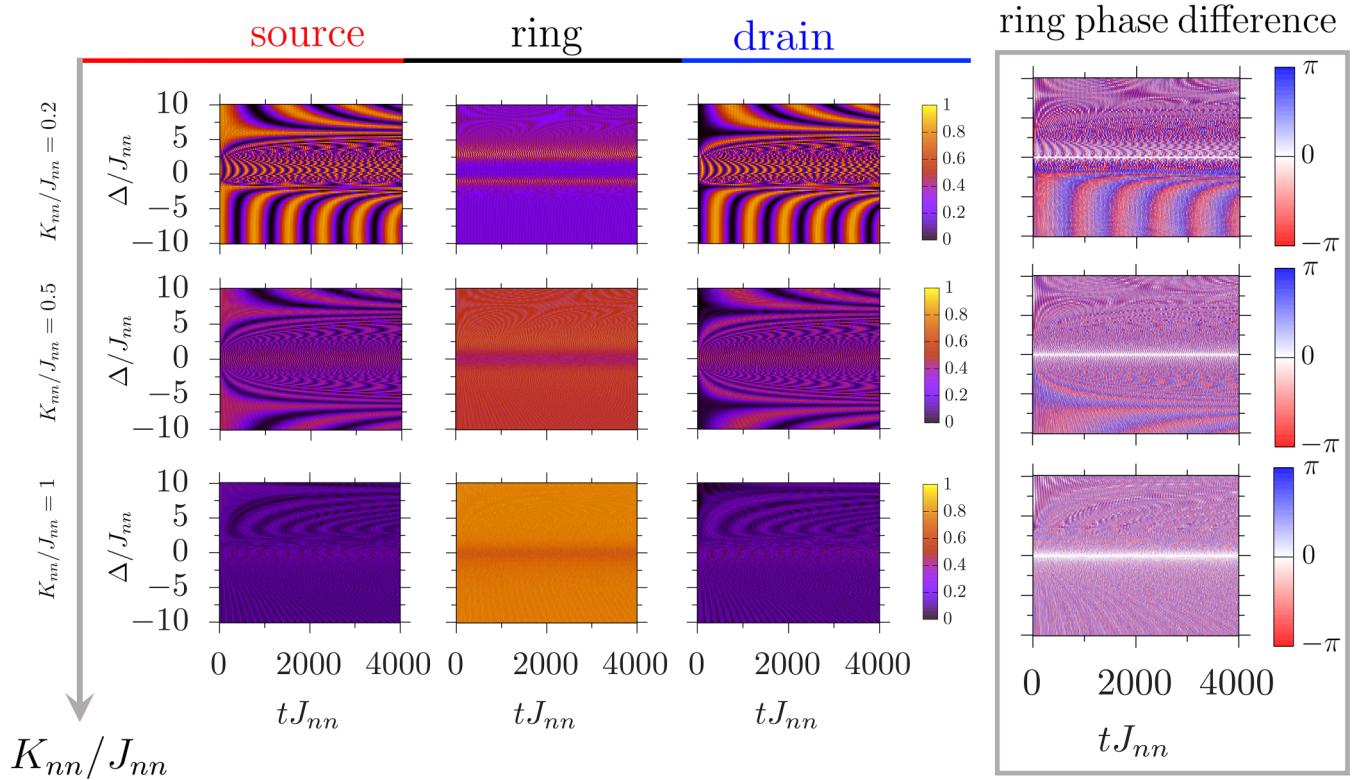


FIG. 14. Left panels: Excitation populations in the source P_S , in the ring P_R , and in the drain P_D for three different values of the leads-ring coupling $K_{nn}/J_{nn} = 0.2, 0.5, 1$, from top to bottom. Far-right panels: Ring phase difference $\delta\phi$ between two opposite sites located in the two arms of the ring for the three values of K_{nn}/J_{nn} considered. Excitation populations and phase difference are plotted as a function of time (x axis) and detuning (y axis). Two equal detunings such that $\Delta_A = \Delta_B = \Delta$ located at $j_A = \lceil N_r/4 \rceil$ and $j_B = \lceil 3N_r/4 \rceil$ are considered. The population values are indicated by the color bar that goes from 0 to 1, and the phase difference by the one that goes from $-\pi$ to π . The number of sites in the ring is $N_r = 14$. The inverse hopping range is $\alpha = 3$.

Indeed, due to the symmetry of the system, the excitation acquires the same phase in the two arms. Differently, if the detunings are opposite, strong phase difference oscillations appear in such a way that they are never zero, except in $\Delta = 0$ [Fig. 13(c)]. Figures 13(b) and 13(d) show the phase difference in a situation in which the distance between the detunings is the same as the one considered in the main text, meaning $j_B - j_A = N_r/2$, but they are located in different positions. As in the main text case, the equal barrier case presents two resonances for Δ_{res} analogous to those considered in the main text configuration; they are easily recognizable by fast phase difference oscillations. However, far from resonance, the dynamics is different and strongly depends on the barrier location. The same applies to the opposite barrier case; there is no resonance, but the nature of the oscillation is different.

APPENDIX F: STRONG-COUPLING DYNAMICS

In the main text, we studied the dynamics in the weak leads-ring coupling regime (in particular, we fixed $K_{nn}/J_{nn} = 0.1$). Thanks to this assumption, some important features of the dynamics could be understood through the study of the isolated ring spectrum. If we increase the coupling, the ring and leads modes are no longer separated, the internal dynamics in the ring becomes comparable with those of the leads, and its population becomes significantly nonzero (see Appendix D 2).

Figure 14 reports the population and phase difference behavior for $\alpha = 3$, in the presence of equal detunings for different values of the leads-ring coupling. Comparing these results with those in Fig. 3 obtained for $K_{nn}/J_{nn} = 0.1$, we can recognize clear differences with respect to the weak-coupling case reported in the main text. First, the ring presents a non-negligible population also for values that do not correspond to resonance between ring eigenstates and the source initial state. As regards the source-drain transport, its velocity is increased far from resonance; between the two resonances, the oscillations lose regularity due to the presence of ring modes that enter the dynamics. Increasing the coupling, the ring becomes more and more populated and the source-drain oscillations are less evident. For $K_{nn}/J_{nn} = 0.5$, independently of the detuning, the spectrum is no longer separated in leads and ring states, and thus the resonance plays a marginal role. The dynamics is characterized by weak source-drain oscillations with a pattern that is almost symmetric for $\Delta \rightarrow -\Delta$ and independent on Δ_{res} . Finally, for $K_{nn}/J_{nn} = 1$, the ring and leads dynamics are exactly comparable; the ring is almost fully populated and the leads are characterized by weak oscillations.

The rightmost panels of Fig. 14 show the phase difference $\delta\phi$ between the sites located on the two arms of the ring. As in the weak-coupling case, $\delta\phi$ follows the population oscillations for different values of K_{nn}/J_{nn} . When $K_{nn}/J_{nn} = 1$, the ring is strongly populated. Although the population in the leads is

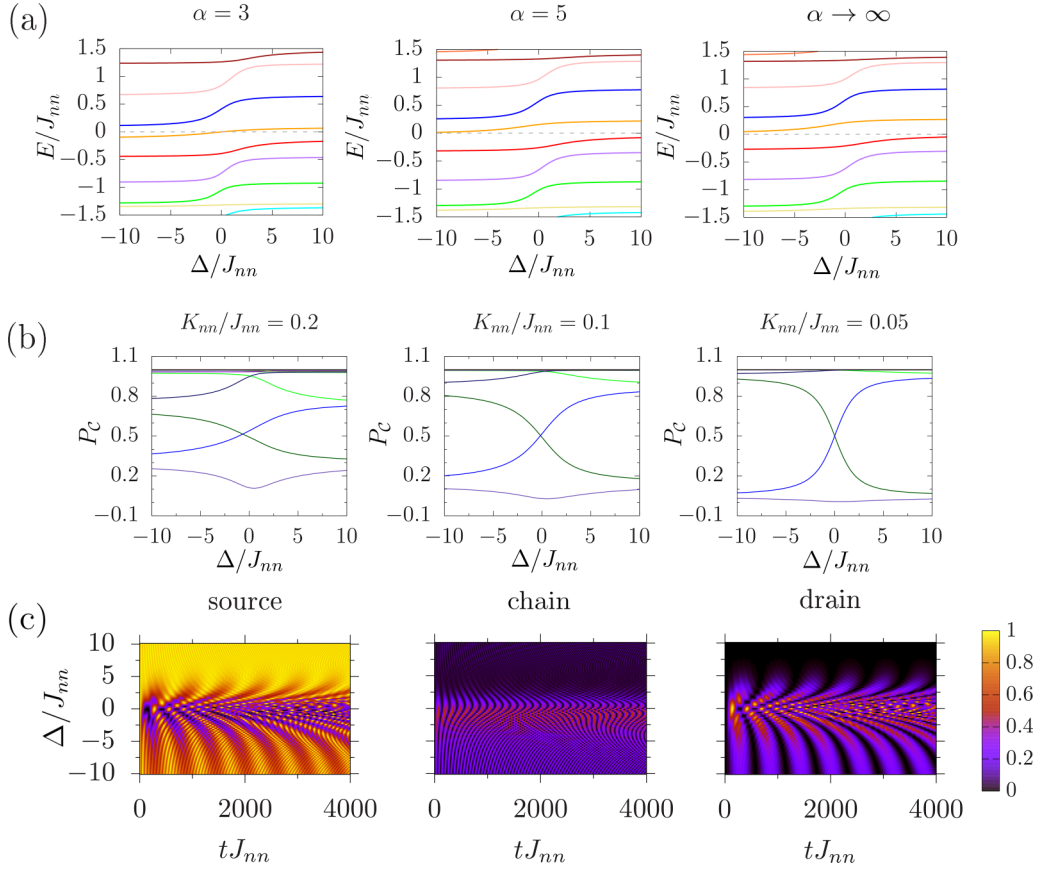


FIG. 15. (a) Uncoupled spectrum close to zero energy, from left to right: $\alpha = 3$, $\alpha = 5$, $\alpha \rightarrow \infty$ which is the nearest-neighbor limit; $K_{nn}/J_{nn} = 0.1$ and $N_c = 14$. (b) Chain populations P_c in the complete spectrum for different values of the ring-leads coupling K_{nn}/J_{nn} ; $\alpha = 3$ and $N_c = 14$. (c) Dynamics of the source, chain, and drain populations (from left to right) for different values of the detuning; the leads-chain coupling is weak $K_{nn}/J_{nn} = 0.05$, the inverse hopping range and the number of atoms are $\alpha = 3$ and $N_c = 14$. In all three panels, a single detuning located at $j_0 = \lceil N_c/4 \rceil$ is considered.

small, the phase oscillations seem to be characterized by the frequency of the source-drain population's oscillations.

Both for the population and the phase difference dynamics, the weak-coupling regime turns out to be the most interesting one in terms of controllability of the source-drain excitation transport through the localized detunings placed in the ring.

APPENDIX G: LINEAR-CHAIN NETWORK

Here we consider an alternative arrangement of the atoms, with respect to that considered in the main text, in which the channel is made of a linear chain of $N_c = N - 2$ atoms. Distances are defined as follows:

$$\begin{aligned} d_{i,j} &= a|i-j|, & d_{S,D} &= d_{S,C} + (N_c - 1)a + d_{D,C}, \\ d_{S,j} &= d_{S,C} + a(j-1), & d_{D,j} &= d_{D,C} + a(N_c - j), \end{aligned} \quad (\text{G1})$$

where a is the lattice spacing in the chain, while $d_{S,C}$ and $d_{D,C}$ are the distances between leads and chain. The sites are labeled in such a way that $j = 1$ is the site connected to the source and $j = N_c$ is the site connected to the drain.

In the nearest-neighbor coupling limit, the channel Hamiltonian can be diagonalized passing first through a Jordan-Wigner transformation and then appropriately rotating the creation and destruction operators. The unperturbed Hamil-

tonian turns out to be [60,61]

$$\hat{\mathcal{H}}_0 = \sum_{n=1}^{N_c} E_n^{(0)} \hat{d}_n^\dagger \hat{d}_n, \quad E_n^{(0)} = 2J \cos\left(\frac{\pi n}{N_c + 1}\right), \quad (\text{G2})$$

where the $d_n^{(\dagger)}$ fermions are superpositions of the $c_n^{(\dagger)}$ fermions (B6),

$$\hat{c}_j = \sqrt{\frac{2}{N_c + 1}} \sum_{n=1}^{N_c} \sin\left(\frac{\pi j n}{N_c + 1}\right) \hat{d}_n. \quad (\text{G3})$$

In this case, the spectrum is not degenerate, and thus the barrier will simply shift the energy levels without splitting any degeneracy. In the case of a nondegenerate spectrum, the first-order correction in the presence of a single detuning located at the position j_0 can be straightforwardly calculated,

$$\Delta E_n^{(1)} = \Delta \langle n | \hat{n}_{j_0} | n \rangle = \frac{2\Delta}{N_c + 1} \sin^2\left(\frac{\pi n j_0}{N_c + 1}\right). \quad (\text{G4})$$

We are interested in the role of the long-range hopping. Figure 15(a) reports the energy spectrum of the uncoupled chain Hamiltonian near the zero-energy value for different values of α . For $\Delta = 0$ and in the nearest-neighbor case, the spectrum is symmetric with respect to $E = 0$; then a linear shift of the levels is caused by Δ . As in the ring case, with a single

detuning, the shift is not sufficient to have a resonance at zero energy in the detuning interval considered. Increasing the hopping range and so decreasing α , the levels are basically shifted downwards in terms of energy. For this reason, for finite α , it is possible that resonances appear. For $\alpha = 3$, we observe a resonance with the zero-energy state at Δ around zero. The presence of a resonance will allow us to state that the ring will be populated during the dynamics.

However, as previously observed, the presence of resonances is not sufficient to obtain complete information on the dynamics. It is also important to understand how the complete spectrum of leads and chain behaves in Δ . In Fig. 15(b), we show the chain population for three different values of the leads-chain coupling K_{nn}/J_{nn} . We can immediately observe that in this case also, for $K_{nn}/J_{nn} = 0.1$, the chain and leads

states are not well separated. In particular, far from resonance, many eigenstates are of the form $|E_{nl}\rangle$ and so the dynamics will not result in coherent oscillations between the source and drain. For $K_{nn}/J_{nn} = 0.05$, the separation is better defined for big values of Δ , while around the resonance, the chain population is $1/2$. Thus, we can conclude that to decouple the leads and chain, we need bigger distances between them with respect to the ring case.

Finally, Fig. 15(c) reports the dynamics of the source, chain, and drain population for $K_{nn}/J_{nn} = 0.05$. In proximity of the resonance, the chain is heavily populated, to the disadvantage of the source. Increasing the value of the detuning and going far from resonance, the transport through the chain is reduced; however, the Δ window in which the chain is populated is not simply a narrow region as in the ring case.

-
- [1] C. W. J. Beenakker and H. van Houten, Quantum transport in semiconductor nanostructures, *Solid State Phys.* **44**, 1 (1991).
- [2] Ya. M. Blanter and M. Büttiker, Shot noise in mesoscopic conductors, *Phys. Rep.* **336**, 1 (2000).
- [3] S. Datta, *Quantum Transport: Atom to Transistor* (Cambridge University Press, Cambridge, 2005).
- [4] Y. V. Nazarov and Y. M. Blanter, *Quantum Transport: Introduction to Nanoscience* (Cambridge University Press, Cambridge, 2009).
- [5] A. D. Stone, Theory of coherent quantum transport, in *Physics of Nanostructures*, edited by J. H. Davies and A. R. Long (IOP Publishing Ltd, 1992), pp. 65–100.
- [6] C.-C. Chien, S. Peotta, and M. Di Ventra, Quantum transport in ultracold atoms, *Nat. Phys.* **11**, 998 (2015).
- [7] D. Stadler, S. Krinner, J. Meineke, J.-P. Brantut, and T. Esslinger, Observing the drop of resistance in the flow of a superfluid Fermi gas, *Nature (London)* **491**, 736 (2012).
- [8] D. Husmann, S. Uchino, S. Krinner, M. Lebrat, T. Giamarchi, T. Esslinger, and J.-P. Brantut, Connecting strongly correlated superfluids by a quantum point contact, *Science* **350**, 1498 (2015).
- [9] L. Corman, P. Fabritius, S. Häusler, J. Mohan, L. H. Dogra, D. Husmann, M. Lebrat, and T. Esslinger, Quantized conductance through a dissipative atomic point contact, *Phys. Rev. A* **100**, 053605 (2019).
- [10] T. Haug, H. Heimonen, R. Dumke, L.-C. Kwek, and L. Amico, Aharonov-Bohm effect in mesoscopic Bose-Einstein condensates, *Phys. Rev. A* **100**, 041601(R) (2019).
- [11] T. Haug, R. Dumke, L.-C. Kwek, and L. Amico, Topological pumping in Aharonov-Bohm rings, *Commun. Phys.* **2**, 127 (2019).
- [12] T. Haug, R. Dumke, L.-C. Kwek, and L. Amico, Andreev-reflection and Aharonov-Bohm dynamics in atomtronic circuits, *Quantum Sci. Technol.* **4**, 045001 (2019).
- [13] Jonathan Wei Zhong Lau, K. S. Gan, R. Dumke, L. Amico, L.-C. Kwek, and T. Haug, Atomtronic multiterminal Aharonov-Bohm interferometer, *Phys. Rev. A* **107**, L051303 (2023).
- [14] L. Amico, M. Boshier, G. Birkl, A. Minguzzi, C. Miniatura, L.-C. Kwek, D. Aghamalyan, V. Ahufinger, D. Anderson, N. Andrei *et al.*, Roadmap on atomtronics: State of the art and perspective, *AVS Quantum Sci.* **3**, 039201 (2021).
- [15] L. Amico, D. Anderson, M. Boshier, J.-P. Brantut, L.-C. Kwek, A. Minguzzi, and W. von Klitzing, Colloquium: Atomtronic circuits: From many-body physics to quantum technologies, *Rev. Mod. Phys.* **94**, 041001 (2022).
- [16] M. Büttiker, Y. Imry, and M. Ya. Azbel, Quantum oscillations in one-dimensional normal-metal rings, *Phys. Rev. A* **30**, 1982 (1984).
- [17] Y. Gefen, Y. Imry, and M. Ya. Azbel, Quantum oscillations and the Aharonov-Bohm effect for parallel resistors, *Phys. Rev. Lett.* **52**, 129 (1984).
- [18] S. Washburn and R. A. Webb, Aharonov-Bohm effect in normal metal quantum coherence and transport, *Adv. Phys.* **35**, 375 (1986).
- [19] D. J. Griffiths and D. F. Schroeter, *Introduction to Quantum Mechanics* (Cambridge University Press, Cambridge, 2018).
- [20] C. Ryu, P. W. Blackburn, A. A. Blinova, and M. G. Boshier, Experimental realization of Josephson junctions for an atom SQUID, *Phys. Rev. Lett.* **111**, 205301 (2013).
- [21] C. Ryu, E. C. Samson, and M. G. Boshier, Quantum interference of currents in an atomtronic SQUID, *Nat. Commun.* **11**, 3338 (2020).
- [22] K. A. Krzyzanowska, J. Ferreras, C. Ryu, E. C. Samson, and M. G. Boshier, Matter-wave analog of a fiber-optic gyroscope, *Phys. Rev. A* **108**, 043305 (2023).
- [23] B. Barrett, R. Geiger, I. Dutta, M. Meunier, B. Canuel, A. Gauguet, P. Bouyer, and A. Landragin, The Sagnac effect: 20 years of development in matter-wave interferometry, *C. R. Phys.* **15**, 875 (2014).
- [24] R. Blatt and C. F. Roos, Quantum simulations with trapped ions, *Nat. Phys.* **8**, 277 (2012).
- [25] C. Monroe, W. C. Campbell, L.-M. Duan, Z.-X. Gong, A. V. Gorshkov, P. W. Hess, R. Islam, K. Kim, N. M. Linke, G. Pagano *et al.*, Programmable quantum simulations of spin systems with trapped ions, *Rev. Mod. Phys.* **93**, 025001 (2021).
- [26] A. Browaeys and T. Lahaye, Many-body physics with individually controlled Rydberg atoms, *Nat. Phys.* **16**, 132 (2020).
- [27] H. Bernien, S. Schwartz, A. Keesling, H. Levine, A. Omran, H. Pichler, S. Choi, A. S. Zibrov, M. Endres, M. Greiner *et al.*,

- Probing many-body dynamics on a 51-atom quantum simulator, *Nature (London)* **551**, 579 (2017).
- [28] D. Barredo, S. de Léséleuc, V. Lienhard, T. Lahaye, and A. Browaeys, An atom-by-atom assembler of defect-free arbitrary two-dimensional atomic arrays, *Science* **354**, 1021 (2016).
- [29] K.-N. Schymik, V. Lienhard, D. Barredo, P. Scholl, H. Williams, A. Browaeys, and T. Lahaye, Enhanced atom-by-atom assembly of arbitrary tweezer arrays, *Phys. Rev. A* **102**, 063107 (2020).
- [30] G. Birkl, S. Kassner, and H. Walther, Multiple-shell structures of laser-cooled 24mg^+ ions in a quadrupole storage ring, *Nature (London)* **357**, 310 (1992).
- [31] D. Kiesenhofer, H. Hainzer, A. Zhdanov, P. C. Holz, M. Bock, T. Ollikainen, and C. F. Roos, Controlling two-dimensional Coulomb crystals of more than 100 ions in a monolithic radio-frequency trap, *PRX Quantum* **4**, 020317 (2023).
- [32] C. Maier, T. Brydges, P. Jurcevic, N. Trautmann, C. Hempel, B. P. Lanyon, P. Hauke, R. Blatt, and C. F. Roos, Environment-assisted quantum transport in a 10-qubit network, *Phys. Rev. Lett.* **122**, 050501 (2019).
- [33] D. Barredo, H. Labuhn, S. Ravets, T. Lahaye, A. Browaeys, and C. S. Adams, Coherent excitation transfer in a spin chain of three Rydberg atoms, *Phys. Rev. Lett.* **114**, 113002 (2015).
- [34] F. Yang, S. Yang, and L. You, Quantum transport of Rydberg excitons with synthetic spin-exchange interactions, *Phys. Rev. Lett.* **123**, 063001 (2019).
- [35] I. Arrazola, J. S. Pedernales, L. Lamata, and E. Solano, Digital-analog quantum simulation of spin models in trapped ions, *Sci. Rep.* **6**, 30534 (2016).
- [36] P. Richerme, Z.-X. Gong, A. Lee, C. Senko, J. Smith, M. Foss-Feig, S. Michalakakis, A. V. Gorshkov, and C. Monroe, Non-local propagation of correlations in quantum systems with long-range interactions, *Nature (London)* **511**, 198 (2014).
- [37] J. G. Bohnet, B. C. Sawyer, J. W. Britton, M. L. Wall, A. M. Rey, M. Foss-Feig, and J. J. Bollinger, Quantum spin dynamics and entanglement generation with hundreds of trapped ions, *Science* **352**, 1297 (2016).
- [38] K. R. Brown, J. Kim, and C. Monroe, Co-designing a scalable quantum computer with trapped atomic ions, *npj Quantum Inf.* **2**, 16034 (2016).
- [39] F. Rajabi, S. Motlakunta, C.-Y. Shih, N. Kotibhaskar, Q. Quraishi, A. Ajoy, and R. Islam, Dynamical Hamiltonian engineering of 2d rectangular lattices in a one-dimensional ion chain, *npj Quantum Inf.* **5**, 32 (2019).
- [40] L. Duca, N. Mizukami, E. Perego, M. Inguscio, and C. Sias, Orientational melting in a mesoscopic system of charged particles, *Phys. Rev. Lett.* **131**, 083602 (2023).
- [41] J. W. Britton, B. C. Sawyer, A. C. Keith, C.-C. J. Wang, J. K. Freericks, H. Uys, M. J. Biercuk, and J. J. Bollinger, Engineered two-dimensional Ising interactions in a trapped-ion quantum simulator with hundreds of spins, *Nature (London)* **484**, 489 (2012).
- [42] B. Yoshimura, M. Stork, D. Dadić, W. C. Campbell, and J. K. Freericks, Creation of two-dimensional Coulomb crystals of ions in oblate Paul traps for quantum simulations, *EPJ Quantum Technol.* **2**, 2 (2015).
- [43] P. Richerme, Two-dimensional ion crystals in radio-frequency traps for quantum simulation, *Phys. Rev. A* **94**, 032320 (2016).
- [44] A. Noguchi, Y. Shikano, K. Toyoda, and S. Urabe, Aharonov-Bohm effect in the tunnelling of a quantum rotor in a linear Paul trap, *Nat. Commun.* **5**, 3868 (2014).
- [45] H.-K. Li, E. Urban, C. Noel, A. Chuang, Y. Xia, A. Ransford, B. Hemmerling, Y. Wang, T. Li, H. Häffner *et al.*, Realization of translational symmetry in trapped cold ion rings, *Phys. Rev. Lett.* **118**, 053001 (2017).
- [46] C. Chen, G. Bornet, M. Bintz, G. Emperauger, L. Leclerc, V. S. Liu, P. Scholl, D. Barredo, J. Hauschild, S. Chatterjee *et al.*, Continuous symmetry breaking in a two-dimensional Rydberg array, *Nature (London)* **616**, 691 (2023).
- [47] G. Bornet, G. Emperauger, C. Chen, B. Ye, M. Block, M. Bintz, J. A. Boyd, D. Barredo, T. Comparin, F. Mezzacapo *et al.*, Scalable spin squeezing in a dipolar Rydberg atom array, *Nature (London)* **621**, 728 (2023).
- [48] M. Endres, H. Bernien, A. Keesling, H. Levine, E. R. Anschuetz, A. Krajenbrink, C. Senko, V. Vuletic, M. Greiner, and M. D. Lukin, Atom-by-atom assembly of defect-free one-dimensional cold atom arrays, *Science* **354**, 1024 (2016).
- [49] V. Lienhard, P. Scholl, S. Weber, D. Barredo, S. de Léséleuc, R. Bai, N. Lang, M. Fleischhauer, H. P. Büchler, T. Lahaye *et al.*, Realization of a density-dependent Peierls phase in a synthetic, spin-orbit coupled Rydberg system, *Phys. Rev. X* **10**, 021031 (2020).
- [50] S. de Léséleuc, D. Barredo, V. Lienhard, A. Browaeys, and T. Lahaye, Optical control of the resonant dipole-dipole interaction between Rydberg atoms, *Phys. Rev. Lett.* **119**, 053202 (2017).
- [51] S. Krämer, D. Plankensteiner, L. Ostermann, and H. Ritsch, QuantumOptics.jl: A Julia framework for simulating open quantum systems, *Comput. Phys. Commun.* **227**, 109 (2018).
- [52] D. V. Averin and Yu. V. Nazarov, Virtual electron diffusion during quantum tunneling of the electric charge, *Phys. Rev. Lett.* **65**, 2446 (1990).
- [53] T. B. Tran, I. S. Beloborodov, J. Hu, X. M. Lin, T. F. Rosenbaum, and H. M. Jaeger, Sequential tunneling and inelastic cotunneling in nanoparticle arrays, *Phys. Rev. B* **78**, 075437 (2008).
- [54] P. Jurcevic, B. P. Lanyon, P. Hauke, C. Hempel, P. Zoller, R. Blatt, and C. F. Roos, Quasiparticle engineering and entanglement propagation in a quantum many-body system, *Nature (London)* **511**, 202 (2014).
- [55] P. Kitson, T. Haug, A. La Magna, O. Morsch, and L. Amico, Rydberg atomtronic devices, [arXiv:2310.18242](https://arxiv.org/abs/2310.18242).
- [56] F. Campaioli, S. Gherardini, J. Q. Quach, M. Polini, and G. M. Andolina, Colloquium: Quantum batteries, [arXiv:2308.02277](https://arxiv.org/abs/2308.02277).
- [57] A. Crescente, D. Ferraro, M. Carrega, and M. Sassetti, Analytically solvable model for qubit-mediated energy transfer between quantum batteries, *Entropy* **25**, 758 (2023).
- [58] P. Jordan and E. P. Wigner, *Über das Paulische Äquivalenzverbot* (Springer, New York, 1993).
- [59] A. De Pasquale and P. Facchi, XY model on the circle: Diagonalization, spectrum, and forerunners of the quantum phase transition, *Phys. Rev. A* **80**, 032102 (2009).
- [60] K. Zawadzki, I. D'Amico, and L. N. Oliveira, Symmetries and boundary conditions with a twist, *Braz. J. Phys.* **47**, 488 (2017).
- [61] S. Hegde, V. Shivamoggi, S. Vishveshwara, and D. Sen, Quench dynamics and parity blocking in Majorana wires, *New J. Phys.* **17**, 053036 (2015).